UNIVERSITY OF LONDON THESIS

Degree PhD Year 2007 Name of Author TRISTAN OLIVER ROBINSON

Gravity currents in the presence of water waves

By

TRISTAN OLIVER ROBINSON

A thesis submitted for the Degree of Doctor of Philosophy

in the University of London

Department of Civil and Environmental Engineering

University College, London

September 2006

ProQuest LLC
789 East Eisenhower Parkway
P.O. Box 1346
Ann Arbor, MI 48106-1346

TO MY MUM AND DAD

ABSTRACT

This thesis describes a laboratory study on the effect of free surface progressive waves on high Reynolds number gravity currents generated by instantaneous release of finite volumes of dense homogeneous fluid. The waves and gravity currents are studied as two-dimensional and the flows across the width of the flume are assumed to be constant.

The engineering applications of this investigation will provide an insight into the processes by which dredging plumes are dispersed and flows propagate into estuaries at the coastline. This investigation examines the process at a fundamental level and gives a summary of the key characteristics and trends of the gravity current in the marine environment.

This work has been carried out in the wave current flume at UCL using a number of advanced flow measuring techniques such as Laser Doppler Velocimetry to measure the orbital velocities of the waves and Particle Image Velocimetry to measure the internal dynamics of the gravity current. The position and density profiles of the gravity current were measured using digital images.

In a static environment a gravity current spreading in two directions has symmetry in shape and distance from the point of release. In the presence of waves, the gravity current fronts propagate with and against the wave direction. The wave motion induces an asymmetry in the shape and rate of propagation of the gravity current fronts. Under certain wave conditions the overall length of the gravity current is found to be unchanged by the presence of the waves and the characteristics of the gravity current are similar to the case in static ambient water. However, in some cases the overall distance is severely modified by the wave motion.

In addition to modifying the propagation rate of the gravity current the wave-induced mean flow modifies the profile of the gravity current head. The direction of the gravity current relative to the wave motion is vital in determining the rate of dispersion and the height of the density current.

ACKNOWLEDGEMENTS

The author would like to thank Dr R.R. Simons and Dr I. Eames for their supervision, advice and guidance throughout the course of study. This projected benefited from the excellent technical support from Mr L. Ansdell and Mr K. Harvey. In particular L. Ansdell who took great interest in the work and provided useful feedback. In addition I am very grateful to Mr S. Justin for his assistance with the computer hardware.

Further thanks to L. Gurr and J. Go for proof reading and all the encouragements during the final stages of my work. The author is also grateful for the advice and help given by J. Ford, W. Fairman and P. Mennell throughout the course of study. In addition my postgraduate peers whom have provided support and relief from the hard work: A. Bahra, J. Rio, O. Jones and D. Sinden.

The author is also grateful for the Studentship awarded by the Engineering and Physical Sciences Research Council, which provided the means to carry out this work.

CONTENTS

List of Figures

List of Tables

List of Symbols

A	Cross-sectional area
b	Path length
B	Buoyancy
c	Concentration
C	Wave velocity
d	Depth
$d_{e^{-2}}$	Laser beam diameter at source
$D_{e^{-2}}$	Laser beam diameter at control volume
$\mathcal{D}$	A vector data set
d_f	Fringe spacing
f_d	Doppler frequency
f_s	Frequency shift
Fr	Froude number
g	Gravitational acceleration
g'	Reduced density
h_c	Gravity current head height
H	Wave height
H_0	Vertical dimension of field view
i	Integers
I	Light intensity
j	Integers
k	Wave number
k_0	Deep water wave number
K	Reflective coefficient
l	Length

l_0	focal length
L	Total length of the gravity current
m	Mass
M	Momentum
M1, M2, M3	Wave probes
n	Integers
0_d	Distance from object
P	Pressure
r	Refractive index
Re	Reynolds number
S	Wave board stroke
t	Time
T	Wave period
u	Horizontal velocity
U	Mean velocity
U_r	Ursell number
v	Vertical velocity
V	Volume
W_0	Horizontal dimensions of field view
x	Horizontal co-ordinate
X	Window reference
x_f	Distance to front of the gravity current
z	Vertical co-ordinate
z_p	Jet length
α_r	Reflective coefficient
η	Free surface wave profile
β	Empirical coefficient
δ	Boundary layer

γ	Theoretical constant
κ	Half angle between two laser beams
λ	Wavelength
λ_0	Deep water wavelength
ν	Kinematic viscosity
$\Omega(t)$	Similarity solutions
ρ	Density
ϕ	Velocity potential
ψ	Stream function
Ψ	Mean stream function
ρ	Density
σ	Angular frequency
θ_c	Angle of gravity current front
θ_h	Horizontal dispersion
θ_v	Vertical dispersion
$\Theta(t)$	Similarity solutions
ε	Extinction coefficient
ζ	Asymmetry of gravity current fronts
$\mathcal{C}$	Centre of the gravity current
$\mathcal{F}(\mu)$	Boundary layer functions
$\mathcal{G}(\mu)$	Boundary layer functions
$\mathcal{H}(\mathcal{X})$	Similarity solutions
$\mathcal{M}$	Mixing factor
$\mathcal{T}$	Light absorbance
$\mathcal{U}(\mathcal{X})$	Similarity solutions
$\mathcal{X}$	Similarity variable

Subscripts:

a	Ambient water
B	Benjamin
box	Box model
c	Gravity current
D	Control volume
E	Viscous flow
f	Free harmonic
HS	Huppert & Simpson
l	Laser component
m	Lagrangian
max	Maximum
min	Minimum
p	Particle
r	Reflective wave
RS	Rottman & Simpson
S	Stokes' drift
SDL	Shin *et al.*
sim	Similarity solution
(1)	First order component
(2)	Second order component
2D	Two-dimensional
3D	Three-dimensional
*	Modified variable/quantity
$-$	Downstream direction
$+$	Upstream direction
l	Lagrangian

Operators:

$\|M\|$	Absolute value
$\mathrm{d}M$	Ordinary differential
$\dot{M}$	Differential with respect to time
ϵ	small increment
∇	Grad
$\hat{\mathbf{M}}$	Vector M
$\overline{M}$	Mean value of M
$\tilde{M}$	Non-dimensional value of M
∂M	Partial differential

CHAPTER 1

INTRODUCTION

1.1 Background

Gravity currents, sometimes called density or buoyant currents, are generated whenever a fluid of one bulk density flows, predominantly horizontally, into an ambient fluid of different density. The density difference between the ambient fluid and the intruding density current is usually due to a difference in temperature, solute composition or particle concentration.

In the present study, the environments under investigation are fluvial and coastal systems; with relevance to naturally occurring phenomena in the ocean such as estuarine flows (figure 1.1), turbidity currents, temperature fronts and oceanic avalanches. In addition, there are a number of man-made activities in the ocean that often generate gravity currents such as dredging, waste dispersion and oil spillage.

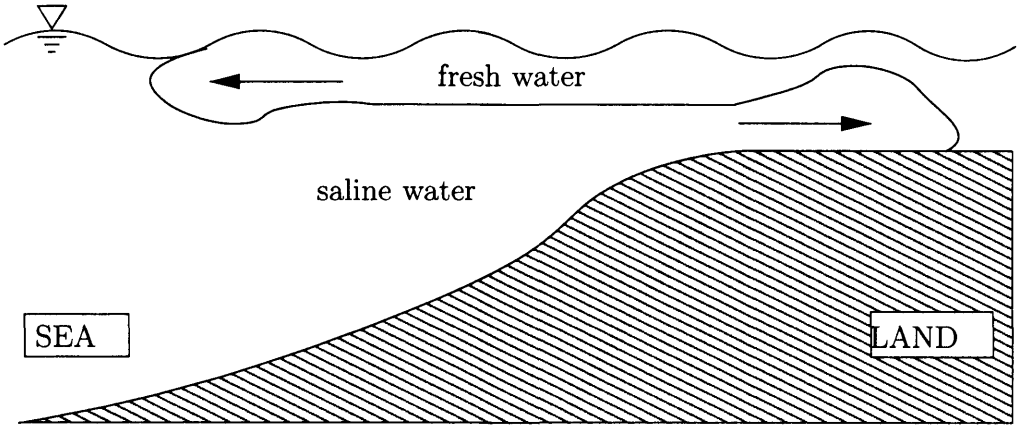

Figure 1.1: *Illustration of an estuarine flow. The fresh water and saline ocean water generate a hydrostatic imbalance that induces the formation of gravity currents.*

A discharge of fresh water into the ocean can produce density driven currents, as illustrated in figure 1.1. The fresh water has a lower density than the saline water and as the two fronts meet, a hydrostatic imbalance is created. The resulting pressure gradient provides the motive force for the generation of the gravity current. In shallow waters as the fresh water is driven upwards and propagates along the free surface an opposing saline current is formed along the bed.

Pritchard & Huntley (2002) have observed buoyant outflows from the estuary of River Teign, Teignmouth, UK. The mouth of the channel is approximately 2m deep and 100m wide. The freshwater flow varies from 2 to 200m^3/s for drought and extreme storm conditions respectively. The peak ebb tidal currents are approximately 5m/s on a Spring tide. Entering Lyme Bay, the discharge current immediately decelerates and observations show the presence of the characteristic gravity type head with velocity in the range 0.1 m/s to 0.25m/s.

The shape of a gravity current is characterised by a rounded head that rises to just over twice the mean height of the interface. Along the interface there are highly turbulent zones where different instabilities are known to form. The rear of the gravity current is referred to as the tail and the density interface here becomes approximately horizontal. These features are common to all different types of physical phenomena that may be classed as gravity currents.

At present there are no models on gravity current that predict the effect of the wave motion on the gravity current dynamics. The models used assume that the characteristics of a gravity current are not modified by the presence of the free surface water waves. This investigation seeks to discover the importance of the wave motion on the dynamics of the gravity current.

1.2 Examples of gravity currents

There are numerous natural and man-made flows that are predominately gravity driven. A list of common examples that have generated recent interest are given

below; a more complete set of examples can be found in Simpson (1997).

- Thunderstorm outflows (Flynn & Sutherland (2004)).
- Smoke fronts (Peters *et al.* (1996)).
- Turbidity currents in the ocean (Kneller & Buckee (2000)).
- Estuarine flows (Zhou (1998) and Pritchard & Huntley (2002)).
- Dredging (Dong & Huang (2004))
- Snow avalanches (Hopfinger (1983))

Atmospheric manifestations of gravity currents include thunderstorm outflows and sea breeze fronts (Flynn & Sutherland (2004)). These natural phenomena generate enormous gravity currents of cold dense air. A photograph of a thunderstorm front, taken from a ship's bow, is shown in figure 1.2. The front produces large changes in the horizontal wind and causes intense areas of turbulence at the density interface.

Figure 1.2: *View of a thunderstorm from the bow of a boat (source: anonymous).*

If a thunderstorm outflow advances over dusty land a dust storm may occur and the front becomes clearly visible. The erosion and the subsequent deposition of the particles suspended in the storm may have devastating consequences to farmland (Simpson (1997)).

Estuaries are regions of transition from river to ocean and are often characterised by an intrusion of fresh water into saline ocean water. According to Hansen & Rattray (1966), the dominant variables in determining the distributions of salinity and circulation within the estuary are: geomorphology, freshwater flow and tides. In this investigation, gravitational estuarine circulations are driven by either clean fresh water, as illustrated in figure 1.1, or heavily contaminated water as shown in the photograph in figure1.3.

Figure 1.3: *A particle laden intrusion into saline coastal ambient water (source: I. Wood (2006) taken from www.cormix.info).*

Sediment-laden fresh water from a river outflow (figure 1.3) may sink to the bottom of the bay if the fresh water discharge has sufficient particles in suspension to give a greater density than the ambient water. When sufficient particles have settled, the density of the discharge will become less than the density of the ambient

fluid. The buoyant fluid will then rise as a plume to the water surface. This phenomenon has been observed by Wright *et al.* (1988) to occur at the delta of the Yellow River in China. Field measurements were carried out of the dispersion of concentrated silts in the Yellow River dominated by gravity-driven underflows. The gravity currents were observed to be 1-4m thick in approximate water depths of 30m. There was both a dense gravity current along the bed and a buoyant current at the surface. There was no records of the wave conditions.

More recently, Wright *et al.* (2001) have extended their study of the Yellow River delta to include the effects of ambient currents and wave motion on the propagation of gravity currents. In this study a scalar maximum orbital velocity was used to analyse the effect of the orbital velocities. It was observed that under specific wave conditions the orbital velocities were the dominant flows and were an important process in determining the speed and resuspension of the laden flows. However, there was no mention or measurements of the wave induced flows and specific characteristics of the gravity current head for different wave conditions.

In addition to naturally occurring gravity currents, there are also those induced by man. These are often associated with serious disasters, causing potential long-term hazardous effects to the environment. Predictions of water column concentrations of suspended sediment are often necessary for environmental impact assessment of point source industrial discharges.

Dredging is the process of lifting sand from one area and dumping some or all of it at a different location. The engineering applications of dredging are: as a source of construction material; to maintain ship routes; for beach recharge; and for land reclamation. In the case of suction dredgers, large volumes of suspended sediment are discharged during the flushing process. This is often carried out in shallow water disposal locations, as illustrated in figure 1.4.

The flushing stage generates a vertical plume of particle-laden flow that plunges to the bottom of the sea and then propagates horizontally, as illustrated in

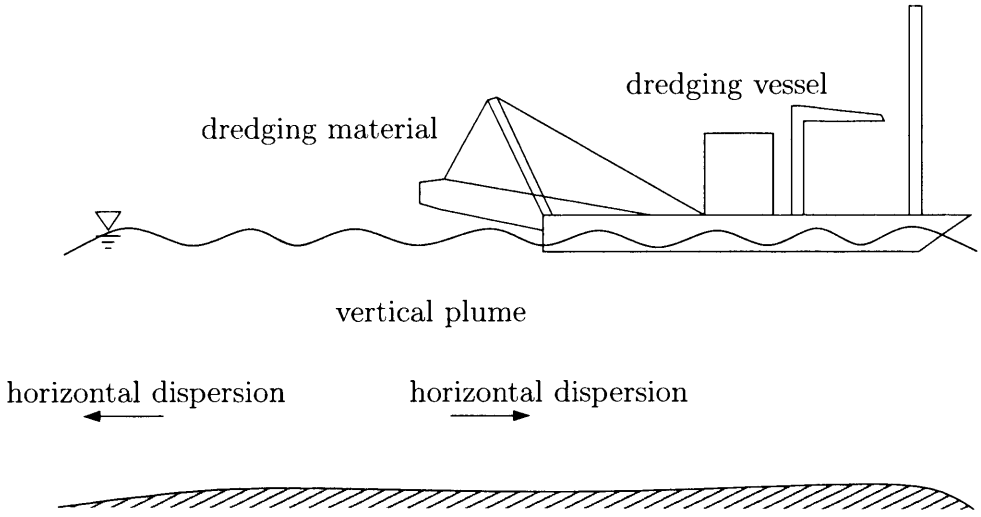

Figure 1.4: *Illustration of a dredging vessel dumping of waste material.*

figure 1.4. An undesired side effect is the propagation and deposition of fine waste materials away from the initial disposal location.

1.3 Historical review

An historical review of gravity currents reveals that the work by Benjamin (1968) is often considered as the fundamental reference on the description of gravity currents. There were a number of studies on gravity currents pre-dating Benjamin's fundamental report. The more important contributions are: Schmidt (1911), von Karman (1940), Keunen (1950) Prandtl (1952) and Keulegan (1958). However, in this investigation the work pre-dating 1968 has not been researched and is assumed to have been accurately summarised in the subsequent investigations. Full references have been given for completeness.

The engineering applications of gravity currents have generated a large number of investigations and the theoretical description of gravity currents is at an advanced stage. Some further developments have been made in cases of gravity current propagating in uniform ambient flow, stratified ambient flows and down an inclined plane. In the presence of waves, however little has been published. The

number of engineering applications of gravity currents occurring in the marine environment makes this an important study to further the understanding of gravity currents and explain a number of natural phenomena found in the environment.

The idealised ocean surface wave theory literature is broad (see reviews by Schwartz & Fenton (1982), Mei & Liu (1993) and Craik (2004)). The theories available, (Stokes (1847), Laitone (1960) and Dean (1965)), provide an accurate description for a large range of regular two-dimensional wave conditions. These waves have the characteristic of a leading order periodic orbital velocity and to second order a wave-induced mean flow, often referred to as mass transport. The concept of mass transport is less well developed and is often overlooked. However, in this investigation the mean velocity will have a direct effect on the propagation of the gravity current.

To the author's knowledge there are no models or laboratory data on the propagation of dense gravity currents in the presence of waves. Due to the large number of applications of gravity currents occurring in the coastal environment this lack of data and available models to predict the propagation of dense gravity currents is an obvious gap in the knowledge that requires further work.

In the absence of available literature on gravity currents propagating in the presence of waves, a review of the existing literature on gravity currents propagating in uniform ambient flows is presented.

1.4 Aims and objectives of the present study

1.4.1 Hydrodynamic processes

The aim of the present study is to describe the characteristics of a gravity current under the effect of regular free surface progressive waves and to address some of the uncertainties in the prediction of density interfaces occurring in the ocean. The study seeks to investigate and quantify the net wave induced flow, its effect on

the propagation of the current, the shape of the front and the indirect additional mixing associated with the wave motion.

This thesis is primarily a laboratory driven research project and discussion of theoretical models is presented as a literature review focusing on the fundamental mechanisms involved. In the absence of relevant theoretical models, the present project will highlight some of the important physical processes occurring and the key elements theoretical models will have to take into consideration.

In order to evaluate the importance of the wave induced flow on the gravity current dynamics, the study addresses the following questions:

1. Does the wave motion have a net effect on the gravity current ?
2. Do surface waves induce additional mixing ?
3. Do the characteristics of a gravity current change in the presence of waves ?
4. What are the engineering implications ?

The present dissertation focuses on the hydrodynamic aspects of gravity currents. Thus many complex and interrelated physical, chemical and biological processes, which affect the full impact of the problem, are not considered. Mackay & McAuliffe (1988) gave a review of these non-hydrodynamic processes.

1.4.2 Outline of thesis

In order to understand the processes that contribute to these areas of interest a review of previous research work, both theoretical and experimental, is presented in chapter 2. Due to the insufficient published articles on the subject, the physical processes of the gravity current dynamics and the wave motion are studied in isolation.

The experimental apparatus and analysis tools are outlined in chapter 3. In the first half of chapter 3 the apparatus, instrumentation and measuring techniques

are described. The flow measuring tools include: video image processing to measure the propagation and shape of the gravity current; Laser Doppler Velocimetry to measure particle velocities of the wave motion; Particle Image Velocimetry to measure the velocity vectors within the gravity current; and Light Induced Fluorescence, to visualise the interface between the gravity current and the ambient flow. In the second half of chapter 3, the specially adapted data analysis techniques are explained and illustrated through typical results.

In chapter 4, laboratory measurements of the wave motion and the propagation of the gravity current in static ambient water are given. The principal aims of this chapter are to highlight the effects of the wave motion and to demonstrate the characteristics of a gravity current propagating in static ambient water. The initial measurements of the propagation of the gravity current in the absence of waves were done as control experiments to ensure that the release method used in this investigation generated consistent gravity currents as previously reported.

In chapter 5, the propagation of gravity currents in the presence of waves is described. Experiments were repeated and compared with the measurements in static ambient water. An initial indication of the effect of the wave motion on the propagation of the gravity current is presented. In addition, the wave-induced oscillation of the gravity current is examined.

The structure and dynamics within the gravity current is presented in chapter 6. Having established the importance of wave motion earlier, this chapter provides a further investigation of the influence of the wave motion on the characteristics of the gravity current and the mechanisms through which the wave motion may alter the propagation of the gravity current.

In chapter 7, the effect of the wave induced ambient flow on the propagation of the gravity current is carried out through a comparison between results from the different measuring techniques. In particular, the importance of the shear layer and the relative propagation direction of the gravity current on the characteristics

of the current. In addition, the dye concentration results are re-examined and compared with the light intensity profiles from the LIF measurements.

The dissertation concludes with chapter 8. This provides an overview of the experimental study, its principal results and suggestions for further work.

Chapter 2

Review of the Physical Processes

2.1 Introduction

In this chapter, a review of the two physical processes under investigation is presented through previously published studies. The chapter begins with a review of the dynamics and properties of free surface progressive water waves generated in a wave flume. The effects under investigation are the orbital oscillation caused by the periodic movement of the free surface profile and the wave induced mean flow.

The review of gravity currents begins with the case of density flow intrusion in static ambient water. The existing models describing the propagation of gravity currents in static ambient water are derived for completeness. This is followed by the application of these models in the case of gravity currents propagating in uniform ambient flows.

2.2 Wave theory for regular periodic free-surface waves

The wave theory literature is quite extensive (see reviews by Schwartz & Fenton (1982), Mei & Liu (1993) and Craik (2004)). However, there are no general solutions as each different system, defined in relation to the water depth and wave parameters described below, usually requires a different mathematical approach to give a realistic prediction of the wave motion. The appropriate wave theory is usually dependent on the following wave parameters: wave height, H, defined as the

vertical distance from the wave trough to wave crest; the wavelength, λ, defined as the distance between successive crests; and the wave period, T, defined as the time between successive crests passing a particular point. A schematic diagram of a typical stable and regular two-dimensional free surface progressive wave is illustrated in figure 2.1. In addition to the wave parameters already given, the other wave properties mentioned in this report are the phase velocity, $C = \lambda/T$, angular frequency, $\sigma = 2\pi/T$, and wave number, $k = 2\pi/\lambda$.

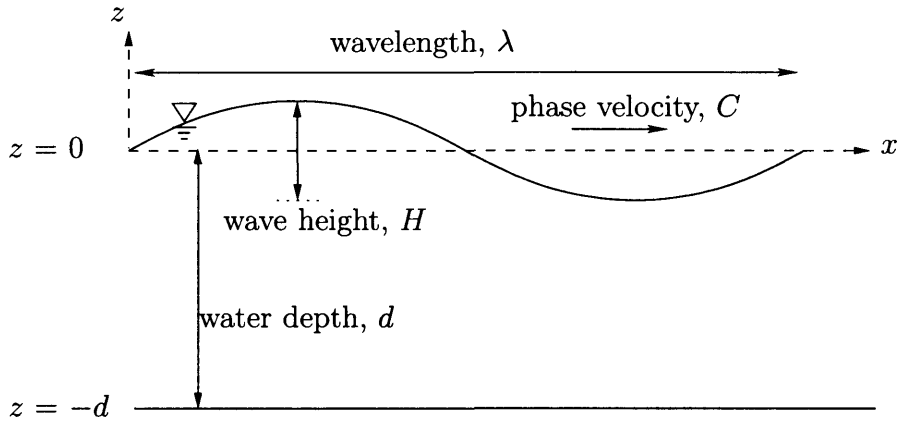

Figure 2.1: *Illustration of a two-dimensional free surface sinusoidal wave.*

Le Mehaute (1976) categorised free surface waves as either deep water, intermediate or shallow water depending on the ratio of wavelength to water depth. These can be written in terms of the dimensionless depth parameter, d/gT^2, and the ratio of water depth to wavelength, where the appropriate wavelength is dependent on the wave regime, see table 2.1.

Classification	d/gT^2	d/λ	Wavelength, λ
Deep water waves	> 0.08	$> 1/2$	$gT^2/2\pi \quad (= \lambda_0)$
Intermediate waves	0.0025 to 0.08	1/20 to 1/2	$\lambda_0 \tanh(2\pi d/\lambda)$
Shallow water waves	$< 1/20$	< 0.0025	$T\sqrt{gd}$

Table 2.1: *Classification of the wave regimes, taken from Le Mehaute (1976).*

Dimensionless parameters are frequently used to characterise free surface waves. The wave height is often expressed in terms of H/gT^2; the wave steepness, H/λ; or relative height, H/d. The water depth is often expressed in terms of the dimensionless depth parameters d/gT^2. Le Mehaute (1976) produced a summary of the ranges of applicability of different wave theories based on the parameters d/gT^2 and H/gT^2. The illustration is reproduced in figure 2.2. As the wave steepness becomes greater, higher order theories are required.

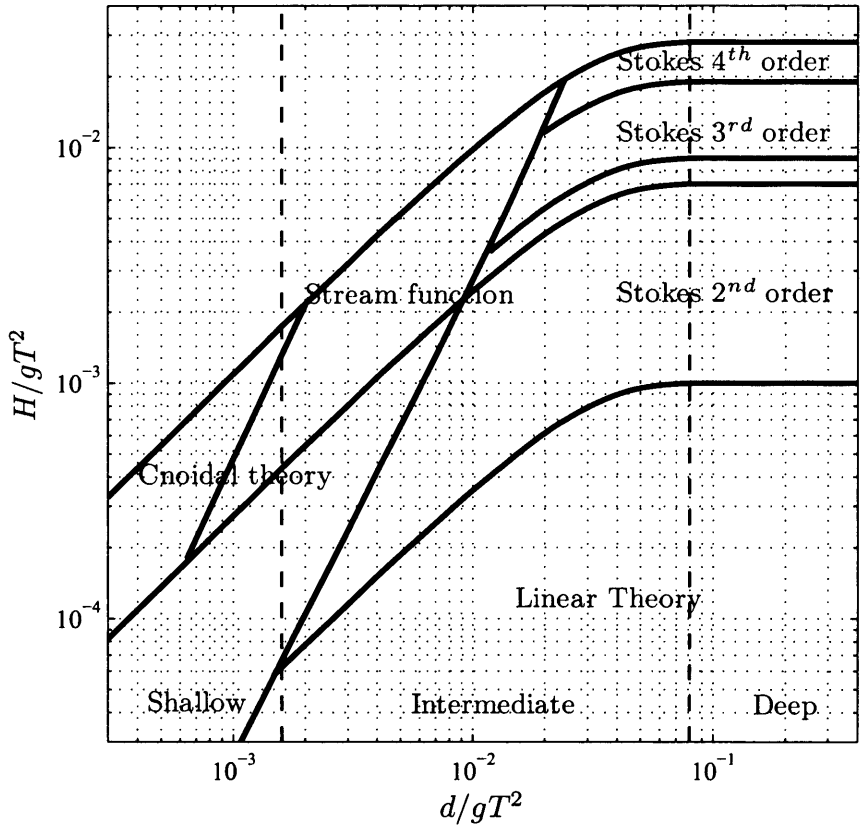

Figure 2.2: *Regions of validity for various wave theories reproduced from the work of Le Mehaute (1976).*

It has been reported by Sarpkaya & Isaacson (1981) that Le Mehaute's wave regime figure was not based on any quantitative investigation and so is somewhat arbitrary. There are other, less well known, wave regime figures such as Dean (1965)'s wave validity figure. Dean used a theoretical closeness method to produce a range of applicability for Cnoidal, Linear and Stokes' 4^{th} order wave theories.

The two figures by Dean (1965) and Le Mehaute (1976) showed similar validity regions and to the author's knowledge, nobody has since disputed the range of wave validity of figure 2.2.

However, during the literature research some discrepancies were found between Le Mehaute's wave theory limits (figure 2.2) and other theoretical validity limits. Researchers have made some progress over the last three decades in 1) determining the appropriate wave breaking condition (see reviews by William (1981) and Shore Protection Manual (1984)); 2) Improving the Ursell number, $U_r = H\lambda^2/d^3$, limit (see reviews Sarpkaya & Isaacson (1981) and Coastal Engineering Manual (2002)); 3) Refining Stokes' 3rd order limit (see review Coastal Engineering Manual (2002)). Small discrepancies were found with the wave-breaking limit, appropriate Ursell number and Stokes' 3rd limit. These small differences are due to differences in the appropriate limiting values, approximations of the intermediate wavelength or reproduction errors. However, more noticeable differences were found at the validity limit of the linear wave theory and Stokes 2nd order wave theory:

1. A wave validity review in the Coastal Engineering Manual (2002) gave the limiting wave steepness value between linear wave theory and Stokes 2nd order theory as:

$$\frac{H}{\lambda} \leq \frac{1}{80}\left(\frac{\sinh^3 kd}{\cosh kd(3+2\sinh^2 kd)}\right), \tag{2.2.1}$$

2. An expansion of the Stokes 2nd order wave theory by Sarpkaya & Isaacson (1981) showed that the applicability of Stokes' theory becomes questionable when:

$$\frac{H}{\lambda} \geq \frac{1}{3\pi}\left(\frac{\sinh^2 kd\tanh kd}{2+\cosh 2kd}\right), \tag{2.2.2}$$

The linear wave validity limit (2.2.1) and the validity limit of Stokes' theory (2.2.2) have been superimposed on Le Mehaute's original wave theory applicability range in figure 2.3. For deep water, the modified linear wave theory limit, (2.2.1), is the same as the original limit. However, there are significant differences in the

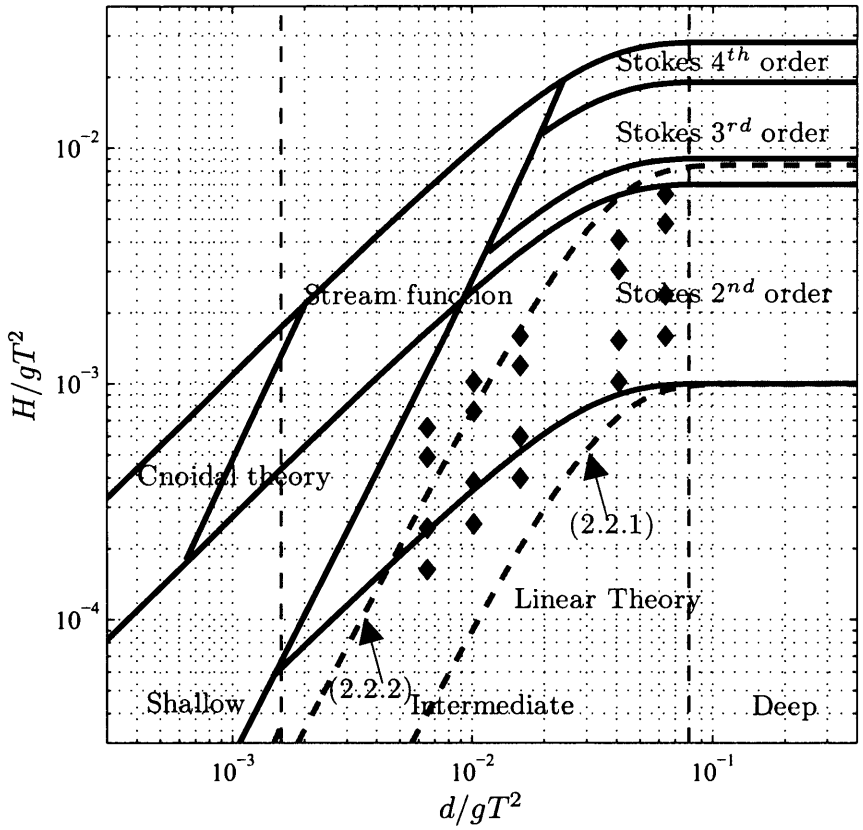

Figure 2.3: *Regions of validity for various wave theories reproduced from the work of Le Mehaute (1976) overlaid with wave theory validity limits* (2.2.2) *and* (2.2.1) *(- -) and the wave parameters for the waves under investigation* (♦).

intermediate water regime. The limit, (2.2.1), predicts a much smaller region of validity for the linear wave theory.

The limit, (2.2.2), predicts that Stokes 2nd order wave theory will decrease in accuracy at a much lower relative wave height than the original limit used by Le Mehaute (1976). This is more noticeable for the intermediate water regime. However, for the deep water regime the new validity limit predicts an only slightly lower relative wave height than the original limit.

The modified validity limits, (2.2.1) and (2.2.2), are important in the present study as the waves under investigation either fall within the linear theory, Stokes' 2nd order or higher order wave theories depending on which validity limits give better approximation.

2.3 Inviscid wave theory analysis

Stokes' theory is based on the assumption that the fluid is homogeneous, incompressible and of uniform depth. The case of a two dimensional wave in Cartesian coordinates $(\hat{\mathbf{x}}, \hat{\mathbf{z}})$, where $\hat{\mathbf{x}}$ is the horizontal axis, $\hat{\mathbf{z}}$ is the vertical axis, is shown in figure 2.1. It is assumed that there is a rigid impermeable bottom at $z = -d$, and at the free surface the elevation is given as $z = \eta(x, t)$, where η defines the free surface vertical profile of the wave dependent on position, x, and time, t. In the absence of waves, it is assumed that the free surface corresponds to $z = 0$.

The flow is irrotational, where both surface tension and viscosity are considered to be not important in the flow dynamics. Following the notation of Acheson (1998) the continuity condition can be written as:

$$\nabla^2 \phi = 0, \tag{2.3.1}$$

where ϕ is the velocity potential function:

$$\nabla \phi = (u, v) \tag{2.3.2}$$

and

$$\nabla = \hat{\mathbf{x}} \frac{\partial}{\partial x} + \hat{\mathbf{z}} \frac{\partial}{\partial z} \tag{2.3.3}$$

for the two dimensional case.

Integrating Euler's momentum equation gives Bernoulli's equation (see Lamb (1932)):

$$\frac{\partial \phi}{\partial t} + \frac{1}{2} \left| \nabla \phi \right|^2 + \frac{P}{\rho_a} + gz = 0, \tag{2.3.4}$$

where P is the pressure, ρ_a is the ambient water density and g the gravitational acceleration.

At the free surface, the boundary conditions are specified in terms of the kinematic and dynamic conditions. The kinematic boundary condition stipulates

that a fluid particle at the water surface will remain on the water surface. Thus, at the free surface, $z = \eta$, the kinematic condition is written as:

$$\frac{\partial \phi}{\partial z} = \frac{\partial \eta}{\partial t} + \frac{\partial \phi}{\partial x}\frac{\partial \eta}{\partial x}, \tag{2.3.5}$$

following the notation by Hughes (1995).

The dynamic boundary condition consists of continuity in the tangential velocities and normal stresses at the air-water interface. Therefore, neglecting surface tension forces, the dynamic boundary condition at the free surface, $z = \eta$, is written as:

$$\frac{\partial \phi}{\partial t} + \frac{1}{2}\left(\left(\frac{\partial \phi}{\partial x}\right)^2 + \left(\frac{\partial \phi}{\partial z}\right)^2\right) + g\eta = 0, \tag{2.3.6}$$

which is determined by Bernoulli's theorem (see Phillips (1980)).

Along the rigid impermeable bottom, $z = -d$, the kinematic boundary condition is applied:

$$\frac{\partial \phi}{\partial z} = 0. \tag{2.3.7}$$

In order to solve the boundary conditions (2.3.5) and (2.3.6), the velocity potential, ϕ, and free surface profile, η, are determined by the sum of the coefficients of the dimensionless parameter, $\epsilon = H/\lambda$, order terms:

$$\phi = \phi^{(1)}\mathcal{O}\left(\epsilon^1\right) + \phi^{(2)}\mathcal{O}\left(\epsilon^2\right) + \phi^{(3)}\mathcal{O}\left(\epsilon^3\right) + \ldots \phi^{(j)}\mathcal{O}\left(\epsilon^j\right), \tag{2.3.8}$$

$$\eta = \eta^{(1)}\mathcal{O}\left(\epsilon^1\right) + \eta^{(2)}\mathcal{O}\left(\epsilon^2\right) + \eta^{(3)}\mathcal{O}\left(\epsilon^3\right) + \ldots \eta^{(j)}\mathcal{O}\left(\epsilon^j\right), \tag{2.3.9}$$

where the dimensionless perturbation parameter, ϵ, corresponds to the wave steepness and is typically much smaller than one. The $\mathcal{O}\left(\epsilon^j\right)$ notation is used to represent the different order solutions, $\phi^{(j)}$ and $\eta^{(j)}$. As the wave steepness order increases the terms in (2.3.8) and (2.3.9) become increasingly smaller in magnitude.

In addition, it is assumed that the velocity potential at the free surface, $z = \eta$, can be represented by a Taylor series expansion about $z = 0$. Following the

notation by Hughes (1995), to second order $\mathcal{O}\left(\phi^{(2)}\right)$, the velocity potential can be written as:

$$\phi(\eta, x, t, \epsilon) = \phi^{(1)}\mathcal{O}\left(\epsilon^1\right) + \left(\phi^{(2)} + \eta^{(1)}\frac{\partial\phi^{(1)}}{\partial z}\right)\mathcal{O}\left(\epsilon^2\right) \tag{2.3.10}$$

The perturbation expressions (2.3.8) and (2.3.9) with the Taylor series, (2.3.10), are substituted into the kinematic, (2.3.5), and dynamic, (2.3.6), conditions. A series of solutions can be derived and known as Stokes' higher order solutions.

2.3.1 Linear theory

The linear wave theory is derived by re-arranging the leading order, $\mathcal{O}\left(\epsilon^1\right)$, terms of the kinematic (2.3.5) and dynamic (2.3.6) boundary conditions applied at $z = 0$ as:

$$\frac{\partial^2\phi^{(1)}}{\partial t^2} + g\frac{\partial\phi^{(1)}}{\partial z} = 0. \tag{2.3.11}$$

The solution to (2.3.11) is known and the derivation can be read in Lamb (1932). Hence, the first order the velocity potential is given as:

$$\phi^{(1)} = \frac{gH}{2\sigma}\frac{\cosh(k(d+z))}{\cosh kd}\sin(kx - \sigma t). \tag{2.3.12}$$

and the dispersion equation is given as:

$$\sigma^2 = gk\tanh kd, \tag{2.3.13}$$

Substituting (2.3.12) into (2.3.6) and to leading order, the free surface profile is given as:

$$\eta^{(1)} = \frac{H}{2}\cos(kx - \sigma t), \tag{2.3.14}$$

where $z = 0$

Substituting (2.3.12) into (2.3.2) and with the use of (2.3.13) gives the horizontal and vertical velocity components:

$$u^{(1)} = \frac{\sigma H}{2}\frac{\cosh k(z+d)}{\sinh kd}\cos(kx-\sigma t), \tag{2.3.15}$$

$$v^{(1)} = \frac{\sigma H}{2}\frac{\sinh k(z+d)}{\sinh kd}\sin(kx-\sigma t), \tag{2.3.16}$$

where $u^{(1)}$ and $v^{(1)}$ are the first order orbital velocities.

To first order, (2.3.15) and (2.3.16), fluid elements beneath the wave surface execute a closed loop as illustrated in figure 2.4. However, to second order, the fluid elements move in the direction of wave propagation because of the slight asymmetry between the velocity at the top of the orbit and the velocity at the bottom.

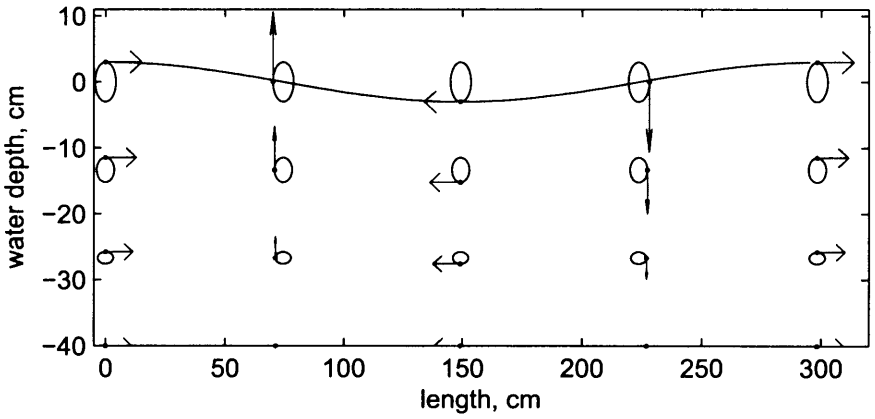

Figure 2.4: *Illustration of the first order orbital circulation for a 1.6s wave period and 6cm wave height in water depth of 40cm.*

2.3.2 2nd Order theory

The second order, $\mathcal{O}(\epsilon^2)$, solutions are dependent on $\phi^{(1)}$ and $\eta^{(1)}$ defined as (2.3.12) and (2.3.14), respectively. The dynamic, (2.3.6), and kinematic, (2.3.5), boundary conditions at the free surface, following the notation by Hughes (1995), are given

as:

$$\frac{\partial^2\phi^{(2)}}{\partial t^2} + g\frac{\partial\phi^{(2)}}{\partial z} = -\eta^{(1)}\left(g\frac{\partial^2\phi^{(1)}}{\partial z^2} + \frac{\partial^3\phi^{(1)}}{\partial z\partial t^2}\right) \\ -2\left(\frac{\partial\phi^{(1)}}{\partial x}\frac{\partial^2\phi^{(1)}}{\partial x\partial t} + \frac{\partial\phi^{(1)}}{\partial z}\frac{\partial^2\phi^{(1)}}{\partial z\partial t}\right), \tag{2.3.17}$$

and,

$$\eta^{(2)} = -\frac{1}{g}\left(\frac{\partial\phi^{(2)}}{\partial t} + \eta^{(1)}\frac{\partial^2\phi^{(1)}}{\partial z\partial t} + \frac{1}{2}\left(\frac{\partial\phi^{(1)}}{\partial x}\right)^2 + \frac{1}{2}\left(\frac{\partial\phi^{(1)}}{\partial z}\right)^2\right). \tag{2.3.18}$$

As (2.3.17) expresses $\phi^{(2)}$ directly in terms of $\phi^{(1)}$ and $\eta^{(1)}$, a solution can be obtained. Once $\phi^{(2)}$ is known a solution for $\eta^{(2)}$, (2.3.18), can be found.

Hence, the second order solutions, $\phi^{(2)}$ and $\eta^{(2)}$, are given as:

$$\phi^{(2)} = \frac{3\sigma H^2}{32}\frac{\cosh 2k(d+z)}{\sinh^4 kd}\sin(2(kx-\sigma t)), \tag{2.3.19}$$

$$\eta^{(2)} = \left(\frac{\pi H^2}{8\lambda}\right)\frac{\cosh(kd)}{\sinh^3(kd)}\left(2+\cosh(2kd)\right)\cos\left(2(kx-\sigma t)\right). \tag{2.3.20}$$

Expressions for the second order velocity components, $u^{(2)}$ and $v^{(2)}$, can be found in Sarpkaya & Isaacson (1981). However, it can be deduced from (2.3.19) that the mean of the second order orbital velocity reduces to zero. The mean velocity remains zero even if this method is extended to higher order terms. Hence, the net observed mean drift must be defined by a different method.

2.3.3 Wave-induced mean velocity

Stokes (1847) was the first to discuss the concept of a net wave-induced velocity and the same analysis is used currently for deep water waves where the inviscid condition is appropriate. The initial objective of Stokes' paper was to investigate the motion of oscillatory waves to second order approximation, illustrating that the wave height does not affect the phase velocity of the wave. Stokes was able to

demonstrate that the forward motion of the particles was slightly greater than the backward motion, by showing that the particles have a progressive motion in the direction of the wave propagation in addition to the oscillatory motion. Stokes, also noted that in the deep water case the wave-induced mean flow decreased rapidly with distance below the free surface.

The displacement of a particle from an initial position, (x_0, z_0) at $t = 0$, is described in terms of Lagrangian velocities, (u_l, v_l), where u_l and v_l are the instantaneous horizontal and vertical Lagrangian velocities, respectively. The horizontal Lagrangian velocity, u_l, is by written mathematically as:

$$u_l = u\left(x_0 + \int_0^t u_l \, \mathrm{d}t, z_0 + \int_0^t v_l \, \mathrm{d}t, t\right), \tag{2.3.21}$$

A standard approximation of (2.3.21) can be written as:

$$u_l \approx u(x_0, z_0, t) + \left(\int_0^t u_l \, \mathrm{d}t\right) \frac{\partial u(x_0, z_0, t)}{\partial x} + \left(\int_0^t v_l \, \mathrm{d}t\right) \frac{\partial u(x_0, z_0, t)}{\partial z}. \tag{2.3.22}$$

A similar perturbation technique, (2.3.8) and (2.3.9), where $\epsilon = H/\lambda$, is used to derive different order Lagrangian velocities. The first order $u_l^{(1)} = u^{(1)}$, where $u^{(1)}$ was derived earlier (see (2.3.15)). Therefore, the first order mean Lagrangian velocity, $\overline{u_l^{(1)}}$, is zero. The second order Lagrangian component, $u_l^{(2)}$, is given as:

$$u_l^{(2)} = u^{(2)} + \left(\int_0^t u^{(1)} \, \mathrm{d}t\right) \frac{\partial u^{(1)}}{\partial x} + \left(\int_0^t v^{(1)} \, \mathrm{d}t\right) \frac{\partial u^{(1)}}{\partial z}, \tag{2.3.23}$$

where $u^{(2)}$ is the second order horizontal velocity and $u^{(1)}$, $v^{(1)}$ are the first order velocity components, (2.3.15) and (2.3.16), respectively. Substituting (2.3.15) and (2.3.16) into (2.3.23) and taking the mean reveals $\overline{u^{(2)}} = 0$, however the other terms in (2.3.23) produce a mean velocity:

$$U_S = \frac{H^2 \sigma k \cosh 2k(z+d)}{8 \sinh^2 kd}, \tag{2.3.24}$$

where U_S is the wave-induced mean velocity, often referred to as Stokes' mean drift.

The analysis by Stokes (1847) was based on an idealised model, where it was assumed that the system consisted of a regular progressive wave train of infinite extent in the horizontal direction. In the case of a wave flume with only a finite number of waves, an additional back flow must develop to ensure that net horizontal drift is zero. The integral of (2.3.24) over the depth calculates the additional element that must be subtracted from Stokes' drift to ensure no net flux. Hence, the Lagrangian mean velocity with zero net displacement is given as:

$$U_{S^*} = \frac{H^2 \sigma k \cosh 2k(z+d)}{8 \sinh^2 kd} - \frac{H^2 \sigma k \coth(kd)}{8kd}. \tag{2.3.25}$$

An illustration of the mean velocities (2.3.24) and (2.3.25) is given in figure 2.5 for a two-dimensional regular sinusoidal wave with 1s wave period and 6cm wave height propagating in a uniform depth, 40 cm, flume. In this case, the kd value is equal to 1.7.

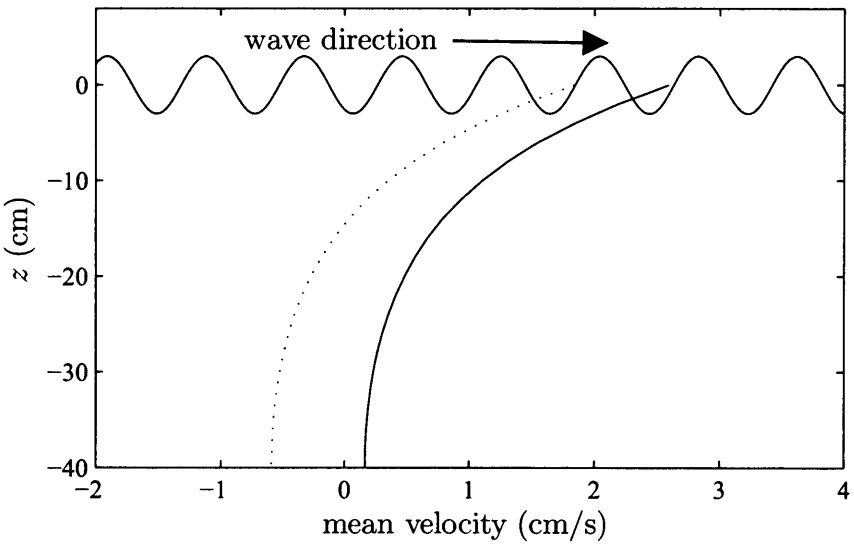

Figure 2.5: *Illustration of theoretical mean drift for T=1s, H=6cm and d=40cm; (——) Stokes drift* (2.3.24), *(· · ·) assuming zero net mean velocity* (2.3.25).

In the inviscid case at the solid boundary the water particles were allowed to 'slip', although the particles on the bed must have the same velocity as the bed

itself. The solution (2.3.24) predicts a positive mean displacement near the free surface and small positive velocity near the bed. The net mean drift for the case in figure 2.5 is $15\text{cm}^2/\text{s}$. In a laboratory wave tank this net mass displacement is not possible because of the finite dimensions of the flume. The revised solution, (2.3.25), predicts a similar velocity profile shifted to the left. Hence, near the free surface the mean velocity is reduced while near the bed, the modified Stokes' drift, (2.3.25), shows a negative mean velocity. In this case the overall net mean drift is zero.

This theory remains the most currently used and accurate model to describe the second order velocities in deep water. The agreement is less good for finite water depths systems, such as wave tanks. Stokes's theory, (2.3.25) (ensuring zero mass displacement), does not explain the large positive velocities close to the bed observed by Bagnold (1946) and Russell & Osorio (1957) in laboratory wave tanks. Therefore, there must be a strong velocity gradient near the bottom, as well as strong vorticity. As the present investigation is primarily interested in the wave effects near the bed where dense gravity currents propagate, the inviscid mean velocity model (2.3.25) is not adequate to describe the mean wave-induced velocity in a laboratory wave tank.

2.4 Viscous dominated wave-induced mean velocity

The classic paper by Longuet-Higgins (1953) derived a new theoretical model describing the second order wave effects observed in wave tanks. The model incorporated viscous boundary layers near the free surface and along the bed. The water is divided into three layers: the free surface boundary layer, the interior core, and the bottom boundary layer, as illustrated in figure 2.6.

The boundary layers are formed by the diffusion of vorticity generated from the constraining surfaces. In the interior region the vorticity contribution is negligible and the flow is considered to remain irrotational assuming small wave heights.

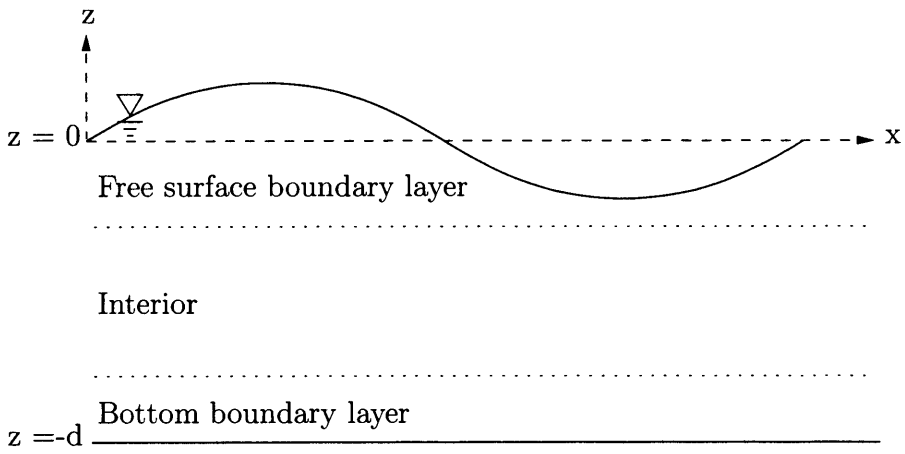

Figure 2.6: *Schematic of the different layers in the flow.*

Longuet-Higgins demonstrated that Stokes' drift, (2.3.24), is not valid in the free surface and bottom boundary layers as the ideal fluid conditions do not give good approximation of the flow. However in the interior flow, Stokes' inviscid velocity potential, (2.3.12), remains valid. In most practical application it is assumed that the boundary layers are of negligible thickness. The boundary layer thickness is defined as:

$$\delta = \left(\frac{2\nu}{\sigma}\right)^{\frac{1}{2}}, \tag{2.4.1}$$

where ν is the kinematic viscosity. A typical value, as given by Douglas *et al.* (1995), of the kinematic viscosity for water is 0.01 cm^2s^{-1}.

Longuet-Higgins (1953) derived a general definition of the wave-induced mass transport, but was unable to derive a general solution. Longuet-Higgins' novel solution for the mass transport was to assign viscous boundary layers near the free surface and bottom; which are then used as boundary conditions to the interior flow. The derivation of the governing equations within the boundary layers may be read in Longuet-Higgins (1953) but for the present purpose only the solutions for progressive waves are presented.

The diffusion of vorticity consists of two parts, the viscous diffusion and the diffusion by convection, and so hence two solutions were proposed: the conduction

and convection solutions. Longuet-Higgins restricted the validity of the conduction solution to very small wave heights. In this case, the interior core of the flow is assumed to remain inviscid, as defined by Stokes, with added boundary conditions at the free surface and along the bed. However, for greater wave heights the equation for the motion in the interior of the fluid becomes quite different. The convection solution is dependent on the conditions at the ends of the tank and an analytical solution remains unresolved. The conduction solution was derived for wave heights smaller than the boundary layer thickness. Huang (1970), Craik (1982) and Swan (1990) argued that the restriction on the wave height could be relaxed. Longuet-Higgins's conduction solution was found to accurately model the mean velocity for most laboratory wave conditions.

Johns (1970) and Jacobs (1984) have investigated wave-induced mass transport with turbulent boundary layers. Jacobs (1984) defined the flow in the boundary layer as turbulent if the Reynolds number, $Re_w \geq 10^4$, where Re_w is given as:

$$Re_w = \frac{u_{\max}^2}{\nu\sigma} \tag{2.4.2}$$

where $u_{\max}$ is the maximum orbital velocity within the boundary layer, (2.4.1), ν is the kinematic viscosity and σ is the angular frequency.

The analysis by Johns (1970) showed that for progressive waves the turbulent boundary layer is independent of the eddy viscosity, resulting in the same mass transport velocity at the outer edge of the boundary layer for both the turbulent and laminar case. This confirms the applicability of Longuet-Higgins's analytical solution, (2.4.19), to turbulent flows. However, Johns found significant differences between the laminar and turbulent boundary layer thickness. For a laminar flow the boundary-layer thickness was found to be about $5\,(2\nu/\sigma)^{\frac{1}{2}}$ whilst for the turbulent case it is about $50\,(2\nu/\sigma)^{\frac{1}{2}}$.

2.4.1 Viscous boundary layers

In proximity to the bed, the oscillatory boundary layer, δ, given as (2.4.1), is very small. For the waves under investigation the boundary layer thickness varies from 0.05cm to 0.09cm. For a number of practical applications the boundary layer is assumed to be negligible and the no slip condition is applied. However, in this investigation this small boundary layer may have important consequences on the propagation of a gravity current with height of 2-5cm. Longuet-Higgins (1953) derived the wave-induced mean velocity in proximity to the bed as:

$$U_m = \frac{H^2 \sigma k}{16 \sinh^2(kd)} \mathcal{F}\left(\frac{z+d}{\delta}\right), \tag{2.4.3}$$

where,

$$\mathcal{F}(\mu) = 5 - 8e^{-\mu}\cos\mu + 3e^{-2\mu}. \tag{2.4.4}$$

The magnitude of the velocity near the bottom boundary is strongly dependent on the wave height and to a lesser extent the relative wave period to water depth. The profile of the horizontal mean velocity is defined by (2.4.4). The no slip condition gives a zero velocity at the bed, which increases rapidly and generates a strong shear layer. This positive velocity explains the strong flow observed in proximity to the bed by Bagnold (1946). The limiting value of (2.4.4) converges to 5 and is used as the boundary condition at the interface between the interior flow and the bottom boundary layer.

Longuet-Higgins assumed that the bottom boundary layer is of negligible thickness and the velocity at the bottom of the flume, $z = -d$, is assumed to be equivalent to the limiting value:

$$U_m\Big|_{z=-d} = \frac{5H^2 \sigma k}{16 \sinh^2(kd)}. \tag{2.4.5}$$

A typical mean velocity profile, (2.4.3), in proximity to the bed is illustrated

in figure 2.7.

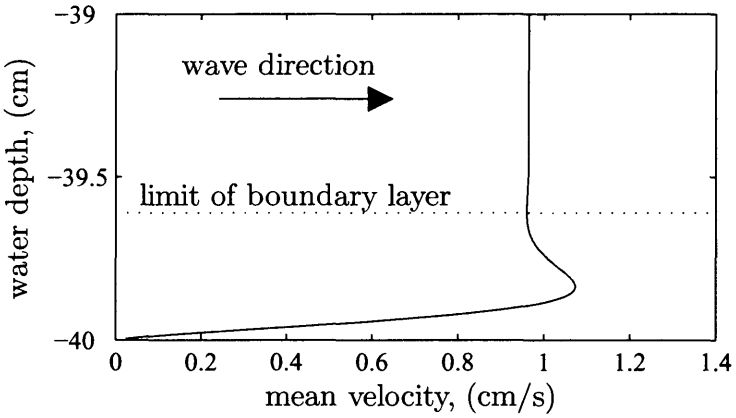

Figure 2.7: *Wave-induced mean velocity,* (2.4.3), *generated at the bed:* $T = 2.5s$, $H = 6cm$ *and* $d = 40cm$.

At the free surface vorticity must be generated as a consequence of a zero tangential shear stress condition (see Batchelor (1967)). Viscous effects cause the vorticity to diffuse into the fluid interior. The velocity gradient is analysed, as it is the boundary condition that is given at the free surface. In this case Longuet-Higgins (1953) provided a boundary layer equation as:

$$\frac{\partial U_m}{\partial z} = H^2 \sigma k^2 \coth(kd)\, \mathcal{G}\left(\frac{z+d}{\delta}\right), \tag{2.4.6}$$

where,

$$\mathcal{G}(\mu) = -1 + e^{-\mu}\cos\mu. \tag{2.4.7}$$

The effect of the vorticity at the free surface is smaller than that along the bottom boundary. The profile of the velocity gradient is dependent on the function (2.4.7), which has a limiting value of -1. Hence, the limiting value of the velocity gradient is given as:

$$\left.\frac{\partial U_m}{\partial z}\right|_{z=0} = -\sigma H^2 k^2 \coth(kd), \tag{2.4.8}$$

A typical profile of the mean velocity gradient (2.4.6) at the free surface is shown in figure 2.8.

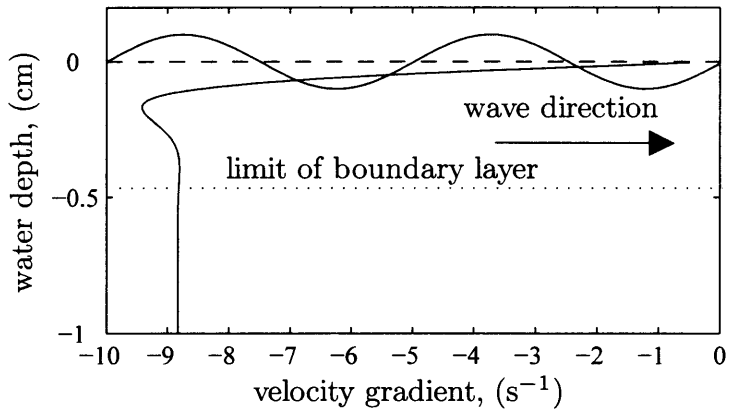

Figure 2.8: *Gradient of the wave-induced mean velocity,* (2.4.6)*, at the free surface:* $T = 2.5s$*,* $H = 6cm$ *and* $d = 40cm$*.*

2.4.2 Irrotational interior core

For the irrotational core of the flow, the governing equation is given in terms of the inviscid velocity potential, (2.3.12). However, the flow is written in terms of stream function, ψ, as the boundary layers flow is rotational and the flow condition for a velocity potential is no longer satisfied. In terms of the horizontal and vertical velocity components, (u, v), the stream function is defined as:

$$(u, v) = \left(\frac{\partial \psi}{\partial z}, -\frac{\partial \psi}{\partial x}\right). \tag{2.4.9}$$

A similar perturbation method used earlier (see (2.3.8) and (2.3.9)) is applied to the stream function ψ. Neglecting higher order terms than ϵ^2, the viscous conduction part of the governing equation was derived by Longuet-Higgins (1953) as:

$$\nabla^4 (\Psi_m) = \nabla^4 \overline{\left(\frac{\partial \psi^{(1)}}{\partial x} \int \frac{\partial \psi^{(1)}}{\partial z} dt\right)}. \tag{2.4.10}$$

The first order stream function $\psi^{(1)}$ is determined by substituting the wave velocity equations ((2.3.15) and (2.3.16)) into (2.4.9). Hence (2.4.10) can be written as:

$$\nabla^4 \Psi_m = \nabla^4 \left(\frac{H^2 \sigma \sinh 2k(z+d)}{\sinh^2 kd}\right), \tag{2.4.11}$$

where four boundary conditions are required in order to derive a unique solution. The boundary at the bed, (2.4.5) and free surface, (2.4.8), have already been derived. The additional boundary conditions are in terms of the stream function Ψ_m. The stream function along the free surface is assumed to be zero and to ensure no net mass displacement, the stream function at the bottom is set to zero. Therefore, the two additional boundary conditions are:

$$\Psi_m\Big|_{z=0} = 0 \quad \text{and} \quad \Psi_m\Big|_{z=-d} = 0. \tag{2.4.12}$$

The stream function (Ψ_m) can be written as $\Psi_m = \Psi_S + \Psi_E$; where Ψ_S is the inviscid stream function and Ψ_E is the viscous stream function. The stream function Ψ_S is defined as $\partial\Psi_S/\partial z = U_S$, where U_S is Stokes' drift (2.3.24). Hence the inviscid stream function Ψ_S is given as:

$$\Psi_S = \frac{H^2\sigma \sinh 2k(z+d)}{16\sinh^2 kd}. \tag{2.4.13}$$

The viscous stream function, Ψ_E, reduces to:

$$\frac{d^4\Psi_E}{dz^4} = 0, \tag{2.4.14}$$

with boundary conditions:

$$\begin{aligned} \frac{\mathrm{d}\Psi_E}{dz}\Big|_{z=-d} &= 3k, & \Psi_E\Big|_{z=-d} &= 0, \\ \frac{\mathrm{d}^2\Psi_E}{\mathrm{d}z^2}\Big|_{z=0} &= -4k^2\sinh 2kh, & \Psi_E\Big|_{z=0} &= \sinh 2kh. \end{aligned} \tag{2.4.15}$$

Integrating (2.4.14) and substituting the conditions (2.4.15) gives the solution for the viscous stream function, Ψ_E, as:

$$\begin{aligned} \Psi_E = \sinh 2kd + 3kz + k^2d^2\sinh 2kd(\mu^3 - 2\mu^2 + \mu) \\ + \frac{1}{2}\sinh(2kd + 3kd)(\mu^3 - 3\mu), \end{aligned} \tag{2.4.16}$$

where $\mu = (z/d)$. Therefore, in terms of the mean viscous velocity, U_E, Longuet-Higgins (1953) derived:

$$U_E = k^2 d^2 \sinh 2kd(\mu^3 - 2\mu^2 + \mu) + \frac{1}{2}\sinh(2kd + 3kd)(\mu^3 - 3\mu) \qquad (2.4.17)$$

The total mass transport, U_m, can be written as the addition of the inviscid drift, U_S, and mean viscous velocity, U_E:

$$U_m = U_S + U_E, \qquad (2.4.18)$$

where U_S is Stokes' drift, (2.3.24), and U_E is the mean viscous flow, (2.4.17). Therefore, the mean wave-induced velocity in a laboratory flume was derived by Longuet-Higgins (1953) as:

$$U_m = \frac{H^2 \sigma k}{16 \sinh^2 kd}\left[2\cosh 2kd(\mu - 1) + 3kh \sinh 2kd(3\mu^2 - 4\mu + 1) + 3\left(\frac{\sinh 2kd}{2kd} + \frac{3}{2}\right)(\mu^2 - 1)\right] \qquad (2.4.19)$$

where $\mu = z/d$.

A plot of the mass transport, (2.4.19), is illustrated in figure 2.9. As the value of kd decreases, the velocity near the free surface increases significantly. Near the bottom, the velocity is negative (against the wave motion) for small kd values. In all cases, the net mass displacement of water is zero.

Russell & Osorio (1957) demonstrated experimentally that Stokes' solution, (2.3.24), describes accurately the observed mass transport for deep water wave conditions and that Longuet-Higgins (1953) conduction solution, (2.4.19), gives a better prediction for longer waves in finite depth models, regardless of the wave height restriction. The experimental observations by Russell & Osorio gave remarkably good agreement with Stokes' inviscid theory and Longuet-Higgins's conduction solution considering both models have a number of approximations.

Author	Nature of investigation	Theory Type	Theory Order	Eulerian/ Lagrangian	Brief description
Stokes (1847)	theory	inviscid	4^{th}	Eulerian	Inviscid theory
Longuet-Higgins (1953)	theory	viscous	2^{nd}	Lagrangian	conduction/convection
Russell & Osorio (1957)	experiment	-	-	Lagrangian	Used suspended particles
Mei *et al.* (1972)	theory/experiments	viscous	2^{nd}	Lagrangian	review
Sleath (1972)	theory	inviscid	4^{th}	Eulerian	4^{th} order solution
Dyke & Barstow (1981)	theory/experiment	viscous	2^{nd}	both	Fourier integral
Swan (1990)	experiment	-	-	Eulerian	LDV measurements
Swan & Sleath (1990)	theory/experiments	viscous	4^{th}	Lagrangian	curvilinear coordinates
Iskandarani (1993)	numerics	viscous	-	Lagrangian	-
Gwinn & Jacobs (1997)	numerics	non-periodic	2^{nd}	Lagrangian	Stuart layer

Table 2.2: *Important contributions to the study of wave induced mean flow.*

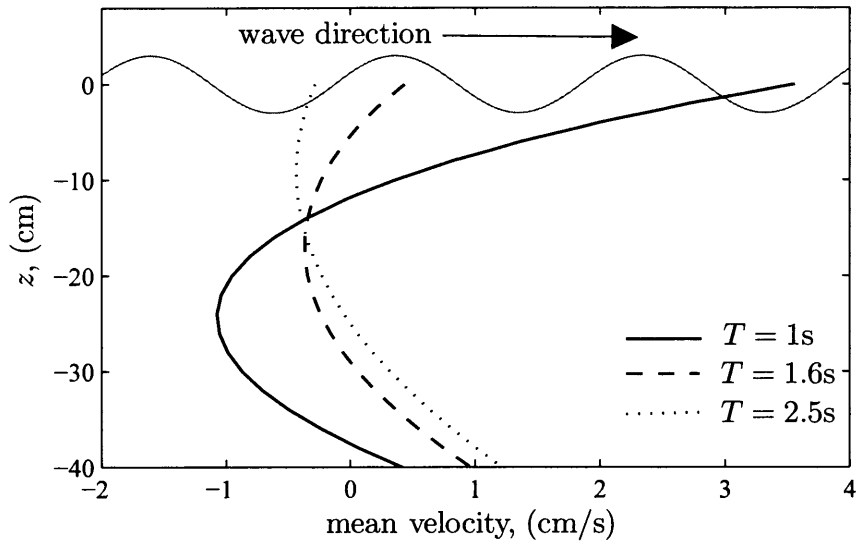

Figure 2.9: *Longuet-Higgins' conduction solution* (2.4.19) *for different wave conditions, kd = (——) 0.8; (- -) 0.9; (· · ·) 0.5 and the wave height, H = 3cm.*

The conduction solution proposed by Longuet-Higgins (1953), however, has been open to criticisms (see table 2.2) as the restriction of small wave heights is generally never implemented in laboratory wave tanks. This restriction implies that the wave heights should be smaller than the oscillatory boundary layer for the vorticity to remain constrained to regions near the boundaries.

Longuet-Higgins (1960) demonstrated experimentally that the vorticity generated by the wave oscillation at the free surface, dispersed inwards into the fluid for wave heights greater than the boundary layer. It was proposed by Longuet-Higgins (1960) that the region affected by the vorticity increases with time. However, no conclusive arguments have been proven whether vorticity spreads into the interior of the fluid or remains in the neighbourhood of the boundary. Swan (1990) showed that the drift velocity varies in respect to both time and distance along the flume. Swan also indicated that the conduction solution gives conflicting results with negative bed velocities and positive vorticity near the free surface, indicating the importance of the convection terms.

Higher order solutions, such as Sleath (1972) and Swan & Sleath (1990), have

shown improvements over the classic Longuet-Higgins solution. However, these models are still based on the same assumptions. Therefore a fourth order solution does not seem appropriate and not worth the extra calculation.

Another improvement in deriving a general solution to the wave induced mass transport is by adopting the curvilinear coordinates at the free surface. Hence, the Navier-Stokes equation can be re-written so that the boundary layer is properly measured from the free surface and not from its mean position, as ordinary perturbation theories demand. This method was used by Ünlunata & Mei (1970) to further validate Longuet-Higgins (1953) conduction solution.

At present, the modified models by Ünlunata & Mei (1970), Sleath (1972), Dyke & Barstow (1981), Swan & Sleath (1990) and Hudspeth & Sulisz (1991) (see table 2.2) have shown different degrees of success. However, all these methods use some type of Fourier integral over wave space and require numerical solutions. This makes the application of these models difficult to compare with experimental results. Hence the most appropriate model to describe the mass transport in laboratory wave tanks remains the original conduction solution by Longuet-Higgins (1953).

In the presence of a random field of ocean surface waves the mean drift velocity in the horizontal direction remains present. However, the analysis by Herterich & Hasselmann (1982) for non-regular wave spectrum has shown considerable differences in the wave-induced flow compared to (2.4.19). In the present study, the waves under investigation are of regular form. However, application to real coastal environments may require some adjustment to the wave induced mass transport.

2.5 Lock release gravity current dynamics

Schmidt (1911) who investigated the effect of the density differences between the ambient flow and density currents carried out the first reported laboratory investigation on gravity currents. The density difference resulted from increasing the temperature of the ambient water. The observations, taken from Simpson (1997) and reproduced in figure 2.10, showed that the density difference defines the shape and rate of propagation of the gravity current.

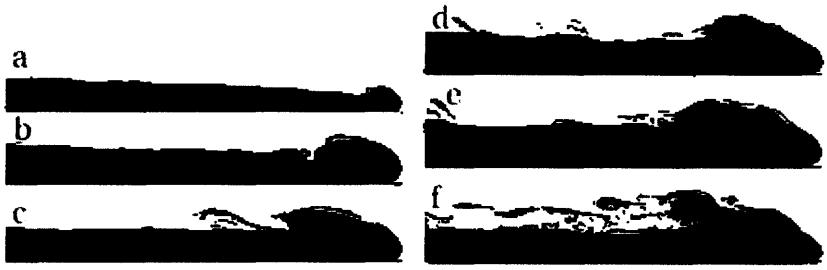

Figure 2.10: *Schmidt used a shadowgraph imagery technique. Temperature difference increases from a few degrees in (a) to* 35° *C in (f). Illustration taken from Simpson (1997)*

Schmidt generated gravity currents with Reynolds number, Re_c, varying from 10 to 1000. A small density difference between the gravity current and ambient water produces viscous dominant currents with Reynolds number ≈ 10, categorised by the small head and little apparent mixing along the density interface (see figure 2.10(a)). As the density difference increases, the buoyancy forces become more significant and the characteristics of the gravity current changes, as illustrated in figure 2.10 by the transition from (a) to (f). Hence, as the density difference is increased the Reynolds number of the gravity current increases. This is due to the increase in the horizontal velocity and height of the gravity current. At a critical Reynolds number of 1000, Kelvin-Helmholtz billow instabilities are generated along the gravity current interface. The instabilities along the density interface induce mixing between the ambient water and gravity current and control the dynamics

of the gravity current head. It has been observed by Schmidt (1911) that further increases in the Reynolds number do not produce additional modifications to the profile of the gravity current. It is these high Reynolds number gravity currents, which are under investigation in the present study. The Reynolds number is defined as:

$$Re_c = \frac{u_c h_c}{\nu}, \tag{2.5.1}$$

hence the condition of high a Reynolds number is satisfied if $u_c h_c > 10\text{cm}^2/\text{s}$.

The engineering motivation behind the initial experimental studies on gravity currents by Keunen (1950) and Keulegan (1958) was to study the density currents caused by the opening and closing of locks that connect fresh-water canals to the sea. Experimental observations were carried out by studying the intrusion of salt water into an expanse of fresh water.

Another application of gravity currents in the marine environment examined by Fannelop & Waldman (1971) and Hoult (1972) is the dispersion of oil spillage at sea. The oil discharge forms a buoyant gravity current that spreads along the water surface. Hoult (1972) incorporated the effects of the wind and tidal currents, but assumed that the wave motion has little contribution to the propagation of the oil spread. Hoult stated at the time that the long-term effect of the wave motion remains unresolved. The effect of the wave motion at present still remains as an unresolved quantity.

The relevance of the propagation of gravity currents in the natural environment has inspired a large number of laboratory and theoretical investigations. The work by Benjamin (1968) is often regarded as the seminal reference on the description of gravity currents. Subsequent investigations have attempted to produce more detailed models, but many of the key characteristics outlined by Benjamin remain valid.

The characteristics of a gravity current head have given rise to most of the investigations on density currents. A schematic of a dense gravity current propa-

gating along a rigid surface is illustrated in figure 2.11 following Benjamin (1968) interpretation.

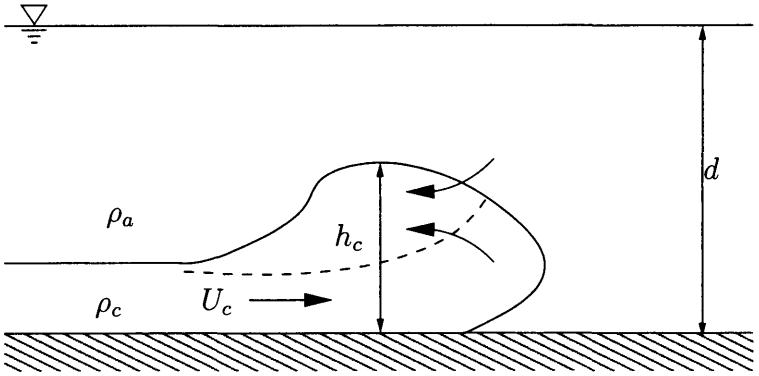

Figure 2.11: *Illustration of the head of a gravity current.*

The head of a gravity current controls the dynamics of the flow. The shape and height of the gravity current head is dependent on the initial volume and the density difference. However, there has been some ambiguity (see review by Marino *et al.* (2005)) in the past regarding the location of the head height. In this report, the height of the gravity current head, h_c, is measured at 15-17cm from the front position of the current. The interpretation of the gravity current height is significant as Benjamin (1968), Huppert & Simpson (1980), Shin *et al.* (2004) and many others use the ratio h_c/d, referred to as the fractional height, to define the front condition of the gravity current.

The standard lock release gravity currents, described by Huppert & Simpson (1980), Rottman & Simpson (1983) and Shin *et al.* (2004), are generated by quickly withdrawing a lock gate. The lock initially separates fluids of contrasting density. In the case of a small finite volume of fluid released in a large expanse of contrasting density, the gravity current has been observed by Huppert & Simpson (1980) and Rottman & Simpson (1983) to go through 4 stages, categorised as: collapse, slumping, inertia and viscous. The collapse stage occurs within a fraction of a second and is assumed to be instantaneous. However, this stage is important due to the significant amount of mixing with the ambient water

As the lock is removed, there is an intrusion of the released fluid into the ambient water. In addition, a disturbance is generated, which propagates in the opposite direction to the gravity current. After the initial collapse, the gravity current propagates horizontally at a constant velocity. This stage is categorised as the slumping stage and its duration is dependent on the time the disturbance wave takes to reflect off the end wall and overtake the gravity current front. After the disturbance overtakes the current head, the gravity current velocity, u_c, decreases with time as $t^{\frac{2}{3}}$. This is categorised as the inertia stage and the dominant forces are buoyancy and gravity. After sufficient time, the gravity current eventually reaches the viscous dominated stage where the gravity current velocity decreases further.

Another type of lock release gravity current, used primarily for intrusion in uniform ambient flows, is generated by releasing a finite volume of high density fluid from a reservoir placed directly above the water surface. The gravity currents released from a reservoir are defined, in this report, as cone release gravity currents. This notation was adopted to make the distinction between the gravity currents generated from a standard lock release and dense water released from a reservoir located above the water surface. It has been observed by Hallworth *et al.* (1998) and Hogg & Huppert (2001) that the cone released gravity currents pass through similar stages to the lock release gravity currents. There is additional mixing during the vertical descent of the released fluid and the duration of the slumping stage is assumed to be zero. The inertia and viscous stages of the gravity current are independent of the release method.

2.5.1 Theoretical description of lock released gravity current

The first theoretical model was established by von Karman (1940), who made two deductions on the basis of Bernoulli's theorem: one, the interface makes a sharp 60^0 angle with the bottom at the front of the gravity current and two, the front

advances at a uniform velocity given by:

$$u_c^2 = 2g'h_c, \tag{2.5.2}$$

where g' is called the reduced gravity and is given as

$$g' = g\frac{g\,(\rho_c - \rho_a)}{\rho_c}. \tag{2.5.3}$$

It was later shown by Benjamin (1968) that the derivation of the constant velocity, (2.5.2), was based on an incorrect assumption. In actual fact, von Karman had found a specific case for a bounded inviscid gravity current. Benjamin (1968) applied a constant pressure distribution along the interface and used perfect-fluid theory (the effects of viscosity and mixing of the fluid were ignored) to produce an alternative velocity expression:

$$u_c^2 = \frac{g'(d^2 - h_c^2)d}{(2d - h_c)h_c}. \tag{2.5.4}$$

Comparison of (2.5.2) and (2.5.4) shows that von Karman's solution is correct for the specific case, $h_c = d/2$, where there is no energy dissipation.

Benjamin (1968) introduced the Froude number, Fr, parameter as a condition at the front of the gravity current. The Froude number is usually used in fluid dynamics as the dominant similarity criterion characterising free surface fluid behaviour. Used primarily to describe open channel flow conditions and is given as the ratio of inertia force to gravity force:

$$Fr = \frac{u_c}{\sqrt{g'h_c}}, \tag{2.5.5}$$

where u_c is the gravity current front speed and $g'h_c$ is the buoyancy force of the gravity current.

The case of no energy loss, (2.5.2), when $h_c = d/2$ gives a critical Froude

number of $\sqrt{2}$. For the general inviscid case, (2.5.4), Benjamin (1968) derived the Froude number as:

$$Fr_{\text{B}} = \left(\frac{2d^2 - 3h_c d + h_c^2}{d^2 + h_c d} \right)^{\frac{1}{2}}. \tag{2.5.6}$$

The Froude number condition at the front of the gravity current has been used in many, if not all, subsequent gravity current investigations and has given rise to a number of theoretical and laboratory investigations defining the appropriate value.

The gravity currents were described by Fannelop & Waldman (1971) and Hoult (1972) to have two (inertia and viscous) distinct time-dependent stages. Initially the buoyancy and inertial forces dominate the gravity current. During this inertia stage, the length scale of the two-dimensional gravity current was found to be proportional to $t^{\frac{2}{3}}$. After sufficient time, the gravity current height decreases and the viscous force becomes more important. The length scale of a viscous gravity current flowing along a rigid bottom was found by Huppert (1982) to be proportional to $t^{\frac{1}{5}}$.

It was later shown by Huppert & Simpson (1980) that the preceding slumping stage in the spreading of gravity currents occurred. This was highlighted by the lack of agreement between Hoult's theoretical model and Keulegan's experimental observations; where the gravity current propagated at constant velocity. Huppert & Simpson (1980) defined the transition from slumping to inertia stage, as the ratio of current height to ambient fluid depth, h_c/d, is less than 0.075. The laboratory investigation by Huppert & Simpson (1980) produced the following empirical condition for the Froude number:

$$Fr_{\text{HS}} = \frac{1}{2}\left(\frac{h_c}{d}\right)^{-\frac{1}{3}} \qquad (0.075 \leq h_c/d \leq 1), \tag{2.5.7}$$

$$Fr_{\text{HS}} = 1.19 \qquad (h_c/d < 0.075), \tag{2.5.8}$$

Rottman & Simpson (1983) found that the description of the gravity current collapsing through series of equal-area rectangles to be incorrect. The more sophis-

ticated approach by Rottman & Simpson (1983) used shallow-water equations with the Boussinesq approximation to derive an approximation of the gravity current dynamics during the inertia phase. The theory assumed that the fluids are inviscid, incompressible and with negligible mixing. However, near the front of the gravity current the shallow-water equations were deemed by Rottman & Simpson to be invalid as the viscous dissipation and vertical acceleration become more important. A front condition was imposed to solve this problem. The solution was presented as a numerical solution of the shallow-water equations and the Froude number as an empirical front condition:

$$Fr_{RS} = \left(\frac{\beta^2 (1-\phi)(2-\phi)}{2(1+\phi)} \right)^{\frac{1}{2}} \tag{2.5.9}$$

where $\phi = h_c/d$ is the fractional height of the gravity current and β is a dimensionless constants determined by experiments. When $\beta^2 = 2$, the empirical Froude number (2.5.9) is identical to Benjamin's theoretical expression, (2.5.6). However, Rottman & Simpson (1983) found that $\beta = 1$ gave a better agreement between theory and observation.

More recently Shin *et al.* (2004) suggested that the energy dissipation inside the flow is unimportant for high Reynolds numbers gravity currents. Shin *et al.* (2004) derived a new relationship for the Froude number assuming conservation of energy as:

$$Fr_{SDL} = \left(1 - \frac{h_c}{d} \right)^{\frac{1}{2}} \tag{2.5.10}$$

The various Froude number definitions (2.5.6) to (2.5.10) have been used in a number of studies as a front condition of the propagation of gravity currents. A comparison of the Froude number expressions, (2.5.6) to (2.5.10), against the fractional height of a gravity current is illustrated in figure 2.12.

In this investigation, two types of theoretical model of the gravity currents are considered. They are the box model and a similarity solution derived from the

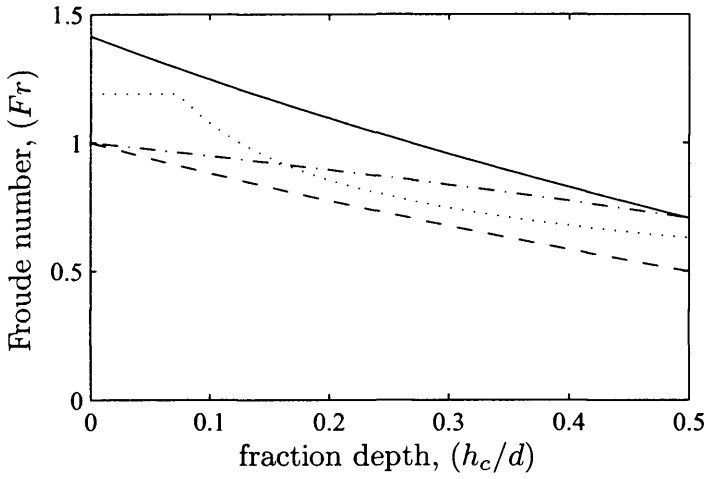

Figure 2.12: *Froude number (Fr) against fractional depth (h_c/d): (——) Benjamin (1968), see* (2.5.6)*; (· · ·) Huppert & Simpson (1980), see* (2.5.7)- (2.5.8)*; (– –) Rottman & Simpson (1983), see* (2.5.9)*; (· – ·) Shin* et al. *(2004), see* (2.5.10).

shallow-water equations. The derivation of both these methods are given below for the propagation of a two-dimensional homogeneous high-density gravity currents propagating in static ambient water.

At present the description of gravity currents is at an advanced stage (see table 2.3). There have been some further improvements in the models described; however, the shallow water model with a front condition remains the most advanced model.

2.5.2 Description of the box model

The box model has been used in a number of studies (see Huppert & Simpson (1980), Dade & Huppert (1995) and Hogg & Huppert (2001)) and comparisons with laboratory tests have shown consistently good agreement. The box model approximates the gravity current as a series of rectangular boxes of constant cross-sectional area, as illustrated in figure 2.13. Hence, the model assumes no mixing between the gravity current and the ambient water and as a consequence the density of the gravity current remains constant. Huppert & Simpson (1980) used the box

Author	Nature of investigation	Theory	Type of fluid released	Dominant force	Length scale	Froude number
Benjamin (1968)	theory/experiments	Bernoulli	air cavity	inertia	t	(2.5.6)
Fannelop & Waldman (1971)	theory	shallow water	solute	inertia/viscous	$t^{\frac{2}{3}}/t^{\frac{3}{8}}$	-
Hoult (1972)	theory/experiment	equation of motion	solute	inertia/viscous	$t^{\frac{1}{2}}/t^{\frac{1}{4}}$	-
Huppert & Simpson (1980)	theory/experiments	box model	solute	slumping/inertia	$t/t^{\frac{2}{3}}$	(2.5.7)/(2.5.8)
Rottman & Simpson (1983)	theory/experiments	shallow-water	solute	inertia	$t^{\frac{2}{3}}$	(2.5.9)
Bonnecaze *et al.* (1993)	theory/experiments	shallow-water	solute/composite	inertia	$t^{\frac{2}{3}}$	1.19
Dade & Huppert (1995)	theory	box model	solute/composite	inertia	-	1.19
Hallworth *et al.* (1998)	theory/experiments	box/shallow water	solute/composite	inertia/viscous	$t^{\frac{2}{3}}$	1.1
Hogg & Huppert (2001)	theory/experiments	box model	composite	inertia	$t^{\frac{2}{3}}$	-
Shin *et al.* (2004)	theory/experiments		solute	inertia	t	(2.5.10)
Marino *et al.* (2005)	experiments	self-similar	solute	inertia/viscous	$t^{\frac{2}{3}}/t^{\frac{1}{5}}$	0.86

Table 2.3: *Important contributions to the understanding of gravity currents.*

model to describe the propagation of the gravity current passing through slumping, inertia and viscous stages by simply modifying the Froude number condition for the different stages.

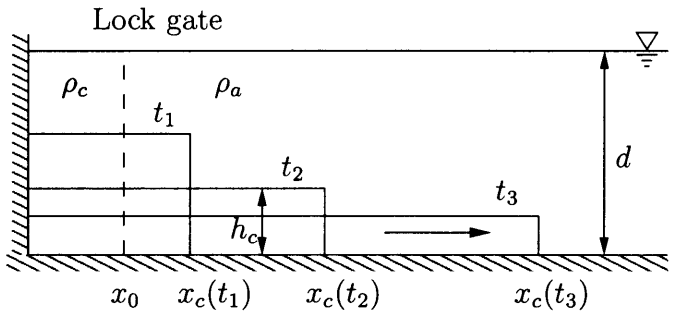

Figure 2.13: *Schematic of the gravity current at different stages.*

In the case of a standard lock release system the initial and subsequent longitudinal cross-sectional area is given as:

$$A = h_0 x_0 = h_c x_c, \tag{2.5.11}$$

where h_0, x_0 are the respective initial height and length of the trapped fluid and h_c, x_c are the respective subsequent gravity current heights and lengths.

For the inertia stage, Huppert & Simpson (1980) defined the gravity current front condition as (2.5.8). Substituting (2.5.11) into (2.5.5) and using the Froude number conditions (2.5.8) gives:

$$x_c^{\frac{1}{2}} \dot{x}_c = 1.19(g'A)^{\frac{1}{2}}. \tag{2.5.12}$$

Integrating (2.5.12) and using the initial conditions, $x = x_0$ at $t = 0$, Huppert & Simpson (1980) found an approximation of the propagation of the gravity current as:

$$x_c(t) = 1.47\,(g'A)^{\frac{1}{3}}\, t^{\frac{2}{3}}, \tag{2.5.13}$$

where it was assumed that the initial length (x_0) was small in comparison to the

length of the gravity current.

The relatively simple box model has been used in more recent investigations (see Hallworth *et al.* (1998) and Hogg & Huppert (2001)) and has also been proven mathematically by Harris *et al.* (2001) to be a good model. The literature review has shown that most studies have derived theoretical models, during the inertia stage of the gravity current front displacement, proportional to $t^{\frac{2}{3}}$. There are however differences in the appropriate coefficient. This is due to the ambiguity in the appropriate front conditions, (2.5.6) to (2.5.10). The method remains the same and can be easily adapted to any of the Froude number front conditions.

2.5.3 Description of the shallow water solution

A more sophisticated approach by Hoult (1972), Rottman & Simpson (1983), Bonnecaze *et al.* (1993) and Hallworth *et al.* (1998) uses shallow-water equations with the Boussinesq approximation to describe the gravity current dynamics. Hoult (1972) first used this method, however in this report the notation by Hallworth *et al.* (1998) has been adopted. The conservation of mass,

$$\frac{\partial h_c}{\partial t} + \frac{\partial}{\partial x}(u_c h_c) = 0, \tag{2.5.14}$$

and conservation of momentum,

$$\frac{\partial}{\partial t}(u_c h_c) + \frac{\partial}{\partial x}\left(u_c^2 h_c + \frac{1}{2} g' h_c^2\right) = 0, \tag{2.5.15}$$

with boundary condition at the gravity current front $x = x_c(t)$ given as:

$$u_c(x,t) = Fr\ (g' h_c)^{\frac{1}{2}}. \tag{2.5.16}$$

Although Rottman & Simpson (1983) showed that there is significant mixing between the gravity current and the ambient water during the slumping stage. The

assumption of constant cross-sectional area is used by Bonnecaze *et al.* (1993) and Hallworth *et al.* (1998). The constant cross-sectional area condition is written as:

$$A_0 = \int_0^{x_c(t)} h_c(x,t)\,\mathrm{d}x, \tag{2.5.17}$$

where A_0 is the initial cross-sectional area, given as the initial volume, V_0, divided by the width of the flume and the gravity current spreads from $x = 0$ to $x = x_c(t)$. Following Harris *et al.* (2001) the length, times and velocities are made dimensionless with respect to $A_0^{\frac{1}{2}}$, $\left(A_0^{\frac{1}{2}}/g_0'\right)^{\frac{1}{2}}$ and $\left(A_0^{\frac{1}{2}}g_0'\right)^{\frac{1}{2}}$.

The dimensionless variables are used to non-dimensionalise (2.5.14) to (2.5.17). And a solution of these dimensionless equations is determined by substituting a non-dimensional similarity variable, $\tilde{\mathcal{X}}$, given as:

$$\tilde{\mathcal{X}} = \frac{\tilde{x}}{\tilde{x}_c(\tilde{t})}. \tag{2.5.18}$$

Hence, the conservation of mass, (2.5.14), can be written as:

$$\frac{\partial \tilde{h}_c}{\partial \tilde{t}} - \frac{\dot{\tilde{x}}_c}{\tilde{x}_c}\tilde{\mathcal{X}}\frac{\partial \tilde{h}_c}{\partial \tilde{\mathcal{X}}} + \frac{1}{\tilde{x}_c}\frac{\partial}{\partial \tilde{\mathcal{X}}}(\tilde{u}_c\tilde{h}_c) = 0, \tag{2.5.19}$$

the conservation of momentum, (2.5.15), can be written as:

$$\frac{\partial}{\partial \tilde{t}}(\tilde{u}_c\tilde{h}_c) - \frac{\dot{\tilde{x}}_c}{\tilde{x}_c}\tilde{\mathcal{X}}\frac{\partial(\tilde{u}_c\tilde{h}_c)}{\partial \tilde{\mathcal{X}}} + \frac{1}{\tilde{x}_c}\frac{\partial}{\partial \tilde{\mathcal{X}}}\left(\tilde{u}_c^2\tilde{h}_c + \frac{1}{2}\tilde{h}_c^2\right) = 0, \tag{2.5.20}$$

and the boundary condition, (2.5.16), at $\tilde{x} = \tilde{x}_c$, can be written as:

$$\tilde{u}_c = Fr\tilde{h}_c^{\frac{1}{2}}, \tag{2.5.21}$$

The similarity method assumes solutions of the form:

$$\tilde{u}_c(\tilde{x},\tilde{t}) = \Omega(\tilde{t})\,\mathcal{U}\left(\tilde{\mathcal{X}}\right), \tag{2.5.22}$$

$$\tilde{h}_c(\tilde{x},\tilde{t}) = \Theta(\tilde{t})\,\mathcal{H}\left(\tilde{\mathcal{X}}\right). \tag{2.5.23}$$

Assuming solutions of the form (2.5.22) and (2.5.23), the coefficients of (2.5.19) and (2.5.20) most remain dimensionless. Substituting (2.5.22) and (2.5.23) into (2.5.19) and (2.5.20) and selecting appropriate $\Omega\left(\tilde{t}\right)$ and $\Theta\left(\tilde{t}\right)$ functions. The similarity solutions, (2.5.22) and (2.5.23), are given as:

Substitute (2.5.22) and (2.5.23) into (2.5.19) and (2.5.20). The functions $\Omega\left(\tilde{t}\right)$ and $\Theta\left(\tilde{t}\right)$ are chosen to give constant coefficients. In this case the similarity solutions, (2.5.22) and (2.5.23), are given as:

$$\tilde{u}\left(\tilde{x},\tilde{t}\right) = \dot{\tilde{x}}_c\,\mathcal{U}(\tilde{\mathcal{X}}), \tag{2.5.24}$$

$$\tilde{h}_c\left(\tilde{x},\tilde{t}\right) = \dot{\tilde{x}}_c^2\,\mathcal{H}(\tilde{\mathcal{X}}). \tag{2.5.25}$$

Hence, the non-dimensional conservation of mass condition, (2.5.19), can be simplified to:

$$\frac{\mathrm{d}\,(\mathcal{U}-\tilde{\mathcal{X}})\mathcal{H}}{\mathrm{d}\,\tilde{\mathcal{X}}} = 0, \tag{2.5.26}$$

with initial condition $\mathcal{U} = 1$ at $\tilde{\mathcal{X}} = 1$ (derived from (2.5.24)). The similarity solution is given as:

$$\mathcal{U}(\tilde{\mathcal{X}}) = \tilde{\mathcal{X}}. \tag{2.5.27}$$

Substituting (2.5.24), (2.5.25) and (2.5.27) into the non-dimensional conservation of momentum, (2.5.20), gives:

$$\frac{\mathrm{d}\,\mathcal{H}}{\mathrm{d}\,\tilde{\mathcal{X}}} = \frac{\tilde{\mathcal{X}}}{2}. \tag{2.5.28}$$

with initial condition $\mathcal{H} = Fr^{-2}$ at $\tilde{\mathcal{X}} = 1$ (substituting (2.5.25) into (2.5.21)).

Hence, the solution of (2.5.28) is given as:

$$\mathcal{H}\left(\tilde{\mathcal{X}}\right) = \frac{\tilde{\mathcal{X}}^2 - 1}{4} + \frac{1}{Fr^2}, \tag{2.5.29}$$

The constant volume condition, (2.5.17) is non-dimensionalised and written in terms of the similarity solutions, (2.5.23). Hence, the non-dimensional front position of the gravity current is given as:

$$\tilde{x}_c(\tilde{t}) = \left(\frac{27Fr^2}{12 - 2Fr^2}\right)^{\frac{1}{3}} \tilde{t}^{\frac{2}{3}}. \tag{2.5.30}$$

Hence in terms of dimensional units, the front position of the gravity current is given as:

$$x(t) = \left(\frac{27Fr^2}{12 - 2Fr^2}\right)^{\frac{1}{3}} (g_0' A_0)^{\frac{1}{3}} t^{\frac{2}{3}}, \tag{2.5.31}$$

The front position, (2.5.31), of the gravity current is defined in terms of the Froude number. Substituting $Fr = 1.19$ into (2.5.31) gives the position coefficient as 1.6, which is of similar order of magnitude than the box model (2.5.13).

2.6 Gravity current propagating in a uniform flow

The initial motivation to study gravity currents in uniform ambient flows by Britter & Simpson (1978) was to examine the mixing caused by the overrun of the gravity current on the less dense ambient water. It was shown experimentally, with the help of a moving floor, that the shear layer suppressed the overrun of less dense fluid. This removed the lobes and cleft instability structures along the gravity current interface. A semi-empirical method by Kranenburg (1993) was developed to take into account the shear layer near the boundaries. The model was quite elementary with a number of assumptions including no mixing and no consideration for the shape of the gravity current heads. However, the model did account for a number of observations found by Britter & Simpson (1978). More recently Hallworth *et al.*

(1998) and Hogg & Huppert (2001) have investigated gravity currents released in a uniform ambient flow.

The standard lock release used by Huppert & Simpson (1980) to generate gravity currents cannot be used in the presence of uniform ambient flows. Hallworth *et al.* (1998) and Hogg & Huppert (2001) used a cone release system positioned in the centre of the flume to generate the gravity currents. The gravity current propagated with two fronts travelling in opposite directions referred to as downstream, x_-, and upstream, x_+. The total length, L, and centre, $\mathcal{C}$, of the gravity current are defined as:

$$L = |x_+| + |x_-|, \tag{2.6.1}$$

$$\mathcal{C} = \frac{1}{2}(|x_+| - |x_-|), \tag{2.6.2}$$

In static ambient water the downstream, x_-, and upstream, x_+, gravity currents propagate, theoretically, with the same velocity magnitude in both directions. Therefore the total length, L, of the gravity current is simply twice the upstream or downstream position of the gravity current fronts and the centre, $\mathcal{C}$, position remains fixed at zero. In the presence of an uniform flow, U_a, this is no longer the case. Hallworth *et al.* (1998) demonstrated that the downstream and upstream gravity current propagate at different velocities. This causes a displacement in the centre of the gravity current. However, Hallworth *et al.* (1998) found that the total length of the gravity current remained the same. An illustration of a dense gravity current propagating in a uniform flow is shown in figure 2.14

Some of main observations by Hallworth *et al.* (1998) and Hogg & Huppert (2001) were:

- Total length, L, of the current increases as $t^{\frac{2}{3}}$.
- The centre, $\mathcal{C}$, of the current propagates downstream at 0.6 times the ambient velocity.

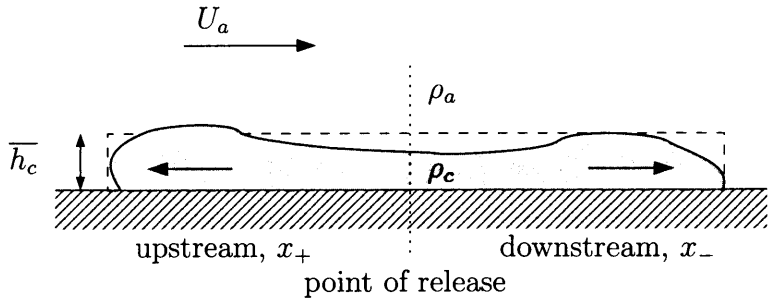

Figure 2.14: *Illustration of the instantaneous released dense current, within a fixed volume parameter.*

- Thicker and faster current propagating downstream compared to an equivalent current propagating in static ambient water.
- The upstream current is significantly retarded and eventually comes to rest.

In the present project, it is assumed that the theoretical models used to describe the propagation of gravity current propagating in uniform ambient flows can be used in the present study. In the presence of a uniform ambient flow the box model and shallow water equation model were adapted by Hallworth *et al.* (1998) to take into account the ambient flow.

2.6.1 Description of the box model

The uniform flow, U_a, is assumed to have a linear contribution to the propagation of the gravity current. Hence, the downstream velocity of the gravity current, $u^*_{c_-}$, can be written as an addition of the gravity current velocity, u_{c_-}, and the uniform ambient flow, U_a. In contrast the upstream velocity, $u^*_{c_+}$, is given as a subtraction of the gravity current velocity, u_{c_+}, and the uniform ambient flow, U_a. The gravity current propagates with velocity $u^*_{c_\mp}$ defined as:

$$|u^*_{c_\mp}| = |u_{c_\mp}| \pm U_a. \tag{2.6.3}$$

Hence assuming similar conditions than the box model described in section 2.5.2 the downstream and upstream positions are given as:

$$|x_{\mp}| = \gamma_{\text{box}} t^{\frac{2}{3}} \pm U_a t, \tag{2.6.4}$$

where,

$$\gamma_{\text{box}} = \frac{1}{2}(3Fr)^{\frac{2}{3}}(g_0' A_0)^{\frac{1}{3}}. \tag{2.6.5}$$

2.6.2 Description of the shallow water solution

Hallworth *et al.* (1998) derived a similarity solution based on a similarity variable dependent on the total length, L, and the centre, C, of the gravity current. Analysis is simplified in this report by assuming that the bed moves at the speed of the uniform ambient velocity, U_a. Following the flume convention the ambient velocity U_a, is taken as a positive mean flow in the downstream direction. The solutions of the shallow water equations, (2.5.14) and (2.5.15), are derived in terms of u_c^*, where $u_c^* = u_c - U_a$. Hence, the two fronts are displaced at equal distances from the point of release. The same dimensionless variables are used to non-dimensionalise (2.5.14) and (2.5.15). However, the non-dimensional similarity variable, $\tilde{\mathcal{X}}$, is given as:

$$\tilde{\mathcal{X}} = \frac{\tilde{x}}{2\tilde{x}_c(t)}, \tag{2.6.6}$$

where $\tilde{x}_c$ is the non-dimensional position of the downstream and upstream gravity current relative to the new frame of reference.

The analysis is similar to the static ambient water case except for the different similarity variable (2.6.6). The new similarity solutions, (2.5.22) and (2.5.23), are

given as:

$$\tilde{u}_c^*(\tilde{x},\tilde{t}) = 2\,\dot{\tilde{x}}_c\,\mathcal{U}(\tilde{\mathcal{X}}), \tag{2.6.7}$$

$$\tilde{h}_c(\tilde{x},\tilde{t}) = 4\dot{\tilde{x}}_c^2\,\mathcal{H}(\tilde{\mathcal{X}}). \tag{2.6.8}$$

where $\mathcal{U} = 1/2$ and $\mathcal{H} = 1/(4Fr^2)$ at $\mathcal{X} = 1/2$. Following similar analysis to Hallworth *et al.* (1998) gives:

$$\mathcal{U}(\tilde{\mathcal{X}}) = \tilde{\mathcal{X}}, \tag{2.6.9}$$

$$\mathcal{H}(\tilde{\mathcal{X}}) = \left(\tilde{\mathcal{X}}^2 - 1\right) + \frac{1}{2Fr^2}, \tag{2.6.10}$$

The similarity solution (2.6.8) and (2.6.10) are substituted into the constant volume condition (2.5.17) with the limits $x_- = -1/2$ to $x_+ = 1/2$. Following similar analysis to Hallworth *et al.* (1998) gives:

$$\tilde{x}_c(\tilde{t}) = \left(\frac{27Fr^2}{6 - Fr^2}\right)^{\frac{1}{3}} \tilde{t}^{\frac{2}{3}}. \tag{2.6.11}$$

In terms of the actual dimensional downstream, x_-, and upstream, x_+, positions, the model predicts that the fronts of the gravity currents are given as:

$$|x_\mp| = \gamma_{\text{sim}}\, t^{\frac{2}{3}} \pm U_a t, \tag{2.6.12}$$

where

$$\gamma_{\text{sim}} = \left(\frac{27Fr^2 g_0' A_0}{6 - Fr^2}\right)^{\frac{1}{3}}. \tag{2.6.13}$$

Hence, the theory, (2.6.12), predicts that the ambient velocity will have a positive contribution to the gravity current in the downstream direction and a negative contribution to the upstream gravity current.

Chapter 3

Experimental Apparatus, Instrumentation and Data Analysis

3.1 Introduction

In order to investigate the contribution of the wave-induced mean flow and the orbital mixing to the dynamics of a gravity driven current, a laboratory investigation was undertaken. The underlying laboratory tests involved the study of second-order wave motion effects that were measured in Eulerian co-ordinates and a Lagrangian observation of the gravity current propagation.

The main experimental apparatus consisted of a wave flume that was specifically adapted to generate density driven flows. The density flows were released at the mid-point of the flume, generating gravity currents spreading upstream and downstream from the point of release. In this investigation downstream relates to the direction of the wave propagation and the direction against the wave motion is referred to as upstream. The measurements of the downstream position were read as negative distances and the upstream measurements as positive values with zero at the point of release. Following this convention, in the presence of waves, the gravity current spreads downstream with negative values in the direction of the wave propagation and upstream with positive values against the wave direction. This system allowed the simultaneous study of the current dynamics with and against the wave motion and determines an overall length of the gravity current.

The overall length, also referred to as the total length, is determined by combining the upstream and downstream position of the gravity current fronts. The asymmetry in the gravity current fronts is determined by the difference between the upstream and downstream positions divided by the overall length. The asymmetry gives a clear indication of the effect of the wave motion on the gravity current dynamics.

The gravity currents were distinguished from the ambient water by adding small amounts of Potassium Permanganate to the released fluid. The initial measurements of the gravity current velocities were done by marking the positions of the gravity current fronts at given time intervals along the side of the flume. These measurements were improved with the use of a video camera running on traverse rails, which allowed the gravity current to be followed along the length of the flume. The post-processing analysis of the images determined the position of the gravity current relative to the release point and the profile of the density interface averaged over the width of the flume. Furthermore, these images were used to measure the density of the gravity current.

The dynamics inside the gravity current head were measured with the aid of a Particle Image Velocimetry (PIV) system. The laser light sheet illuminated a thin vertical planar profile of the gravity current. The method relies on tracking the displacement of particles, illuminated by the laser, between pairs of images. An additional benefit of the PIV system was that the laser light sheet could be reconfigured for Light Induced Fluorescence tests.

3.2 Experimental Apparatus

3.2.1 Description of the wave flume

The experiments were carried out in the UCL wave-current flume, schematically illustrated in figure 3.1. The flume consists of a 1450cm long channel with wave

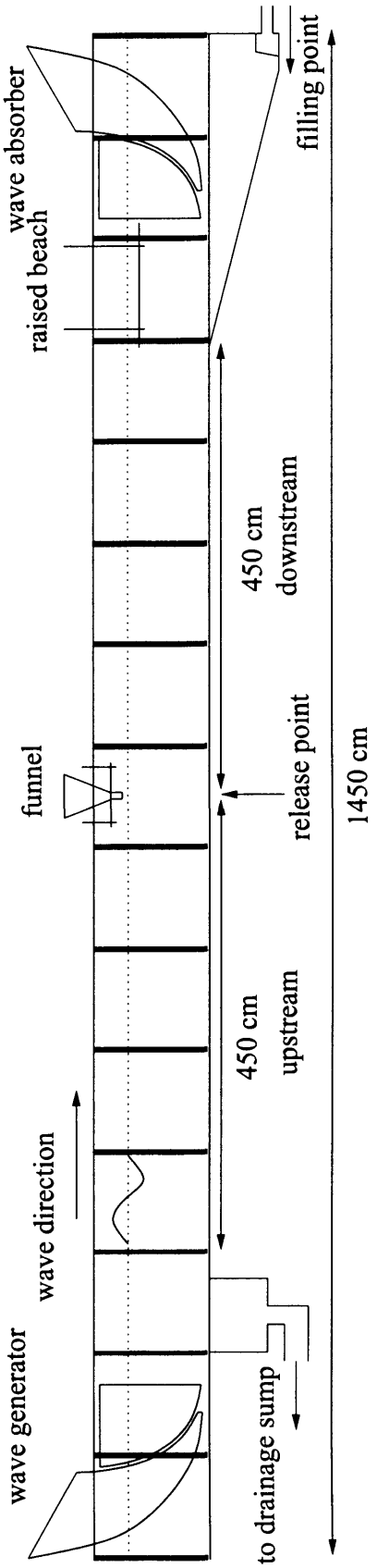

Figure 3.1: *Wave-current flume at UCL, Civil Engineering. Approximate dimensions: 1450cm×45cm×65cm.*

generators located at either end, providing a 900cm long test section. The sidewalls of the flume are constructed from 1 cm thick plate glass. The bed consists of 183cm long and 45.7cm wide cast aluminium sections. The flume is supported along its full length by an iron structure, with U-shaped cast aluminium sections providing support at 91.5cm intervals. The water supply is taken from a storage tank located 1600 cm above the laboratory level. The flume was filled via a 15cm diameter supply pipe. Once the flume was full, the water was allowed to settle for 24 hours before the tests were carried out. This filling process minimised the residual circulation within the flume and removed any air bubbles present in the water.

3.2.2 Description of the wave paddles

The wave flume has the peculiarity of having wave paddles at both ends. This allows waves to be generated at one end of the flume by one paddle and absorbed at the other end by the second paddle. In this study, the waves were generated upstream and absorbed downstream from the release point.

The free surface water wave parameters are generated under computer software control. The wave period and wave height are specified with the use of the WAV language, developed by Edinburgh Design, see Rogers & Bolton King (1997). In addition to a single sinusoidal motion, the paddles are able to superimpose a number of sinusoidal waves of different periods and heights at different phases thus allowing the generation of regular and non-regular waves.

It was found that for the short wave periods (<1s) the downstream wave paddle was unable to absorb a sufficient proportion of the wave energy. This produced the undesired effect of wave reflections. This problem was more apparent for large wave heights (>6cm) where waves reflected off the downstream paddle. After sufficient time the reflected waves resulted in the generation of standing waves. In the less extreme cases, the reflected waves proved disruptive to the wave motion and formed non-uniform and unsteady wave conditions. This problem was resolved

by installing a horizontal perforated plate, 178cm long and 2cm thick, covering the width of the flume. The plate was positioned 38cm from the downstream paddle and was suspended 6cm from the free surface in still water. This ensured that the raised beach remained submerged at all times during the wave oscillation. The plate reduced the size of the incident wave sufficiently that the small residual wave was absorbed by the downstream paddle. A schematic of the plate, also referred to as a raised beach, in the wave-current flume is shown in figure 3.2.

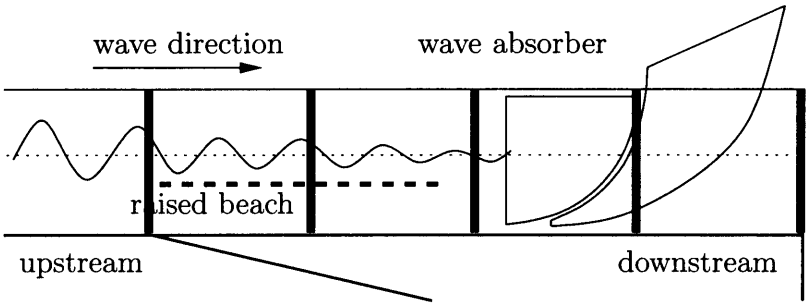

Figure 3.2: *Illustration of the raised beach at the downstream end of the flume.*

3.2.3 Specification of the flume coordinates

A specially designed tape measure was positioned along the length of the flume to measure the propagation of the gravity current. The origin of the tape corresponds to the release point of the density fluid and following the flume convention a negative distance was adopted in the downstream direction and a positive distance in the upstream direction.

The measurements of the gravity current propagation were restricted to the areas between the supporting pillars located at approximately 91.5cm intervals along the length of the flume. This divided the test section into 9 measuring windows. There was one central window at the point of release, $X = 0$, and four downstream and four upstream windows. The start and end positions of the measuring sections at each window, relative to the point of release, are shown in

table 3.1.

Window No.	1		2		3		4	
Range	Start	End	Start	End	Start	End	Start	End
Upstream, x_+ (cm)	55	133	145	225	235	315	328	405
Downstream, x_- (cm)	-55	-135	-145	-221	-235	-313	-325	-405
Reference, X, (cm)	± 55		± 145		± 245		± 325	

Table 3.1: *Position of the windows along the flume.*

The restriction of measuring the gravity current between the supporting pillars becomes more apparent when studying the video captured image of the gravity current; as the pillars prevented measurements of the gravity current front. In the description of the gravity currents it was, sometimes, more convenient to divide the measurements according to the reference values, X, given in table 3.1.

3.2.4 Homogeneous Density flows

Homogeneous density flows are generated by producing a temperature- or chemical-induced density contrast between two fluids. In this investigation, the preferred method of increasing the water density was to dissolve industrial salt in water. Preliminary temperature controlled tests proved unreliable as it was not possible to take a definitive temperature reading at the point of release and sufficient control on the water density was not available. However, the use of temperature allowed for buoyant gravity currents to be generated.

The use of industrial salt was found to produce more reliable measurable densities. These high-density currents were generated with industrial salt consisting of 99% pure Sodium Chloride. In contrast, it was found that standard kitchen salt modified the opacity of the water. This was an undesired side effect, particularly in determining density concentrations of the gravity current. In contrast, the industrial salt did not modify the water clarity.

The density of a gravity current is usually given in terms of the reduced gravity, defined as (2.5.3), which is a function of the densities of the ambient water, ρ_a, and of the fluid introduced, ρ_c. The water densities ρ_a and ρ_c were measured using a gravimetric bottle. Measuring the density for a number of water samples produced a linear relation between the Sodium Chloride concentration and reduced density (see figure 3.3). The concentration values are given as grams/cm^3 or grams/cm^2 per unit width.

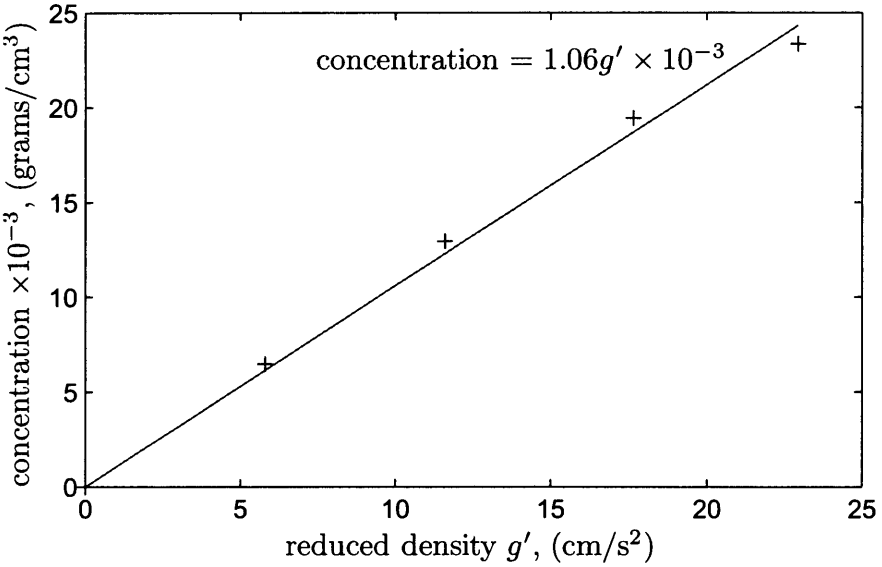

Figure 3.3: *Relation between Sodium Chloride concentration and reduced density.*

The detrimental effect of the salt on the wave flume was not ignored. The water in the flume was flushed to waste and the flume was rinsed daily after experiments.

3.2.5 Release of high density fluid

Release of a fluid into an ambient water of different density can be generated in a laboratory by a number of different methods. These methods are generally categorised as either continuous or lock release. This study concentrates primarily on lock release gravity currents. The lock release gravity currents are sudden

discharge of a finite volume of fluid into the ambient water. The conventional lock release method used by Huppert & Simpson (1980) and Shin *et al.* (2004), consists of a barrier separating the two fluids of different density, which can be lifted instantaneously to generate a density interface and, hence, induce a gravity current. However, this method could not be used in this investigation as the wave motion had to be fully established before the second fluid is introduced into the wave flume. This problem was rectified by using a method similar to Hallworth *et al.* (1998) for the case of gravity currents released in uniform ambient flow. The method consisted of releasing the dense fluid from a funnel located above the water surface. Precautions were taken to ensure the fluid was released on the centre line and the distance between the water surface and funnel outlet was minimised. The funnel outlet had a 3.4cm diameter. A schematic of the release mechanism is shown in figure 3.4.

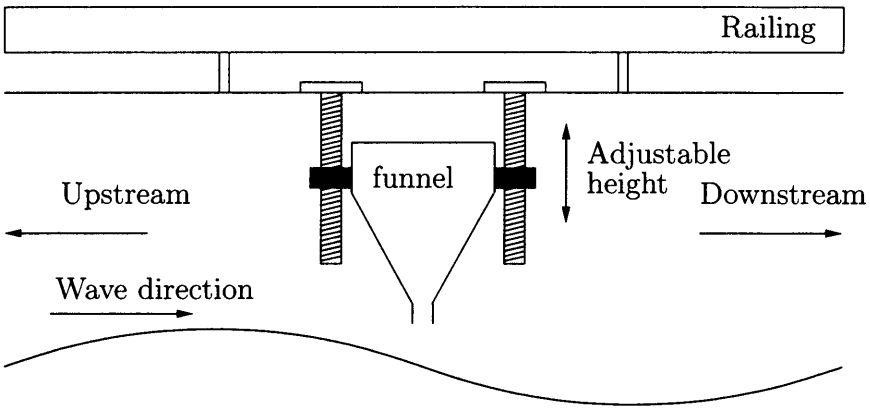

Figure 3.4: *Schematic diagram of the release mechanism.*

A nominal time of 30 minutes was given for the wave motion to become fully developed before the density fluid was released into the flume. Swan (1990) showed that once established the wave-induced velocity remains stable. This is in agreement with the preliminary laboratory observations in the present study.

3.3 Instrumentation

3.3.1 Wave probes

The free surface waves were monitored using resistance-type wave probes. These are simple robust devices that measure the wave height from the electrical current passing between pairs of parallel vertical stainless steel wires partly submerged in the water. The probes are energised with a high frequency voltage and the electrical resistance observed between the wires is proportional to the depth of immersion. In the presence of waves, analysis of the voltage measurements yields the oscillating free surface profile.

In the present study, four wave probes were placed along the length of the flume. These were denoted as S for static, M1 for mobile 1, M2 for mobile 2 and M3 for mobile 3, as illustrated in figure 3.5. The static probe was at a fixed position, located at the downstream end of the flume and was used as the reference probe. The mobile probes were grouped to form one independent unit with fixed spacings that could be moved along the length of the flume, as illustrated in figure 3.5. The distance between the mobile probes remained constant over time: M1 to M2 was 20cm and M2 to M3 was 40cm. A tape measure fixed along the side of the flume established the exact location of the probes relative to the wave generator.

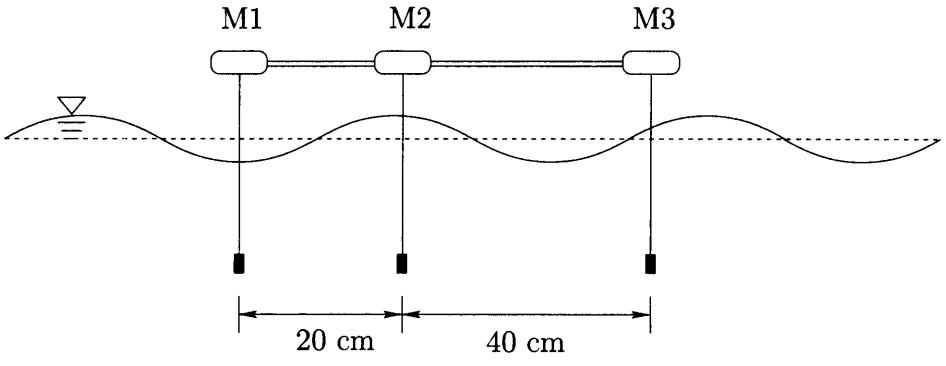

Figure 3.5: *Schematic of the mobile wave probes M1,M2 and M3.*

The voltage output produced by the wave probes was analysed through wave monitor modules and fed to a data acquisition board, DT9801-EC, connected to a computer. The data acquisition board has a resolution of 12 bits and an input range ±10 Volts. The data acquisition board was configured to have 8 differential analogue inputs, although in this investigation, only 4 channels were used. The software, DT Measure Foundry, was used to visualise and capture the signal from the wave probes. An example of the measured voltages from the four probes is shown in figure 3.6, demonstrating that the voltages measurements are not affected by random electronic noise.

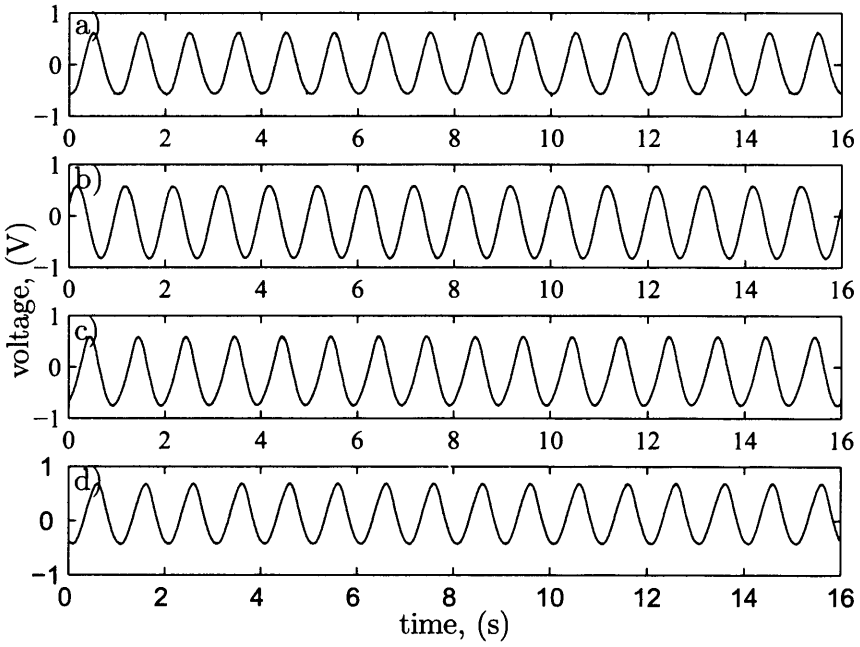

Figure 3.6: *Analogue signal for the four wave probes, for a 1s wave period and an approximate 6cm wave height: a) S1, b) M1, c) M2 and d) M3.*

3.3.2 Laser Doppler Velocimetry

Laser-Doppler Velocimetry (LDV) is a method for measuring fluid velocities by detecting the Doppler frequency shift of laser light that has been scattered by small particles moving in the flow. The Doppler frequency shift is the difference

between that of the incident laser beams and the scattered light frequencies. The particles can be a natural pollutant found in the water although more commonly artificial pollutants are added to the flow.

The technique was first used in water flows by Yeh & Cummins (1964) and has since seen significant improvements, in the signal processing, in particular. A review of the advances in LDV can be read in Tropea (1995). The technique remains a complicated procedure and requires some understanding of the basic principles. A more complete review of the theory is described by Durst *et al.* (1981).

An incident laser beam is split into two beams of the same frequency and intensity, and re-focused to intersect at a point in the flow, as illustrated in figure 3.7.

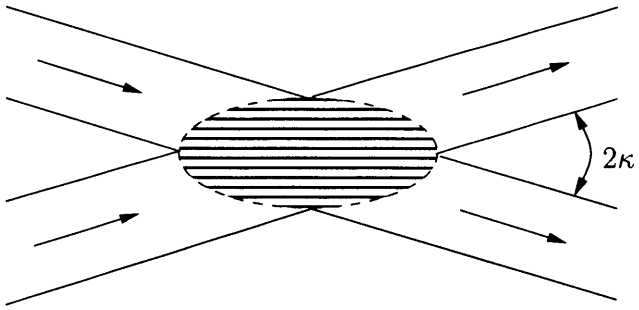

Figure 3.7: *Schematic of a measurement volume and the interference fringe pattern (Durst* et al. *(1981)).*

The point of intersection is referred to as the measurement volume or the control volume. The dimensions of the control volume were given by Durst *et al.* (1981) as:

$$d_D = \frac{d_{e^{-2}}}{\cos\kappa}, \tag{3.3.1}$$

$$l_D = \frac{d_{e^{-2}}}{\sin\kappa}, \tag{3.3.2}$$

$$h_D = d_{e^{-2}}, \tag{3.3.3}$$

where d_D = width, l_D = length, h_D = height of the control volume. The volume,

V_D, of the control volume is then given as:

$$V_D = \frac{\pi d_{e^{-2}}}{6 \cos\kappa \sin\kappa}, \tag{3.3.4}$$

where $d_{e^{-2}}$ is the diameter of the laser beam at the control volume. Durst *et al.* (1981) have shown that the laser beam divergence is very small and at the measurement control volume, the diameter of the beam is given as:

$$d_{e^{-2}} = \frac{4\lambda_l l_0}{\pi D_{e^{-2}}}, \tag{3.3.5}$$

where λ_l is the beam wavelength, l_0 is the focal length and $D_{e^{-2}}$ the initial diameter of the light beam. The diameter, $D_{e^{-2}}$, of the laser light beams usually varies between 0.01cm and 0.5cm depending on the optics at the source. An advantage of laser as opposed to white light is the small divergence of the laser beams compared to white light.

The intersection of two coherent light beams generates a pattern of dark and light bands called interference fringes. These are either parallel, as shown in figure 3.7, or elliptical. Assuming the two beams intersect at an angle of 2κ, the dark fringes are separated by:

$$d_f = \frac{\lambda_l}{2 \sin\kappa}. \tag{3.3.6}$$

As a particle crosses these fringes, the intensity of light scattered varies at a rate directly proportional to the velocity of the particle. If the particles are of appropriate diameter, shape and specific gravity for the fluid under investigation the particles follow the flow path of the fluid. Ensuring that the particles diameter do not interfere with the fringes the fluid velocity is inferred from the measured particle velocity.

The amplitude of the signal burst varies with time and provides a measure of the particle velocity perpendicular to the fringe pattern. The frequency of the

amplitude modulation is given by Durst *et al.* (1981) as:

$$f_d = \frac{2v_p}{\lambda_l} \sin \kappa \tag{3.3.7}$$

where v_p is the particle velocity.

The signal output consists of a Gaussian pedestals plus a burst of Doppler sine waves. The Doppler frequency, f_d, is relatively small in magnitude, of the order of $10^6 Hz$, compared to the laser source, which is of the order of $10^{14} Hz$. Modern electronics are able to pick out these frequencies. The techniques involve the subtraction of the scattered laser light beam frequency from the total frequency, leaving a signal that oscillates at the Doppler frequency see figure 3.8.

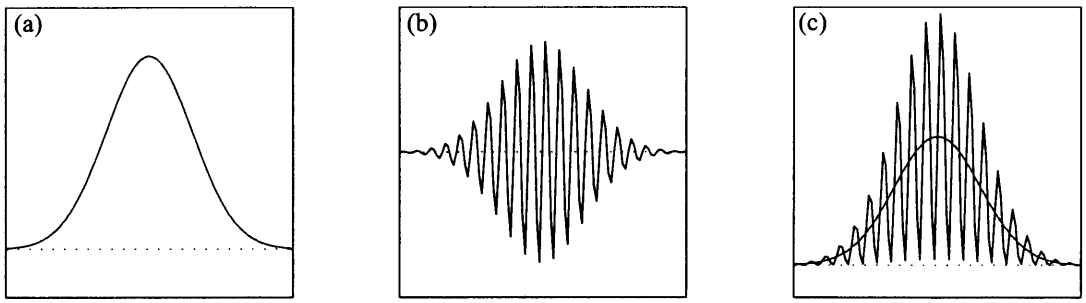

Figure 3.8: *Component of a laser burst: (a) Pedestal, (b) Doppler shift (c) Doppler burst (pedestal + Doppler shift).*

A disadvantage of LDV is that the Doppler frequency, f_d, depends only on the magnitude of the particle velocity, v_p, and not the direction. To correct this directional ambiguity, the frequency of one incoming beam is shifted by a known value called the frequency shift.

This technique can also be used to improve the quality of the measured velocities as certain particle trajectories fail to provide good signal. The number of measurements is increased when the velocity vectors are perpendicular to the fringes and decreased when the angle between the velocity and fringes approaches zero. Frequency shifting adds cycles to a Doppler burst by moving the fringes with

respect to the fluid. If the fringe velocity is large in comparison with flow velocities, even particles travelling parallel to the fringes will produce an adequate number of cycles.

The system at UCL consists of an INNOVA 70C 5-Watt Argon-ion laser and a two-component TSI laser anemometer, with the option of measuring orthogonal velocity components independently. The two-colour dual beam LDV system was set to measure the horizontal and vertical velocity components. The velocity components were identified by the laser beams wavelengths. The properties of the laser beam and size of the control volume, V_D, are given in table 3.2.

Laser colour	Wavelength, λ_l, $\times 10^{-6}$ (cm)	Beam diameter, $d_{e^{-2}}$, $\times 10^{-3}$ (cm)	Fringe distance, d_f, $\times 10^{-6}$ (cm)	Volume, V_D, $\times 10^{-3}$ (cm^3)
Green	51.45	17	53	7.66
Blue	48.80	68	50	7.26

Table 3.2: *Laser beam specifications for* $\kappa = 2.8°$, $l_0 = 51.2cm$ *and* $D_{e^{-2}}=47 \times 10^{-3} cm$.

The green and blue beams from the argon ion laser were each split and refocused to form two mutually orthogonal dual-beam systems. The scattered light was collected by a pair of photo-detectors, one accepting only blue light and the other accepting only green light. The system operated in backscatter mode, with both focusing lenses and photodetector in the laser head. The signals were processed by the TSI IFA-650 signal processor. Small amounts of Titanium (IV) dioxide were added to the water to improve the data burst rate. A schematic of the current LDV system is shown in figure 3.9.

The system transfers the laser light beam to the laser head via a fibre optic cable. Fibre optic cables are able to transmit light over long distances with little power attenuation. In addition, they are fairly flexible and robust. Compared to prisms, which can be used to deliver the laser beams to the test area, fibre optic

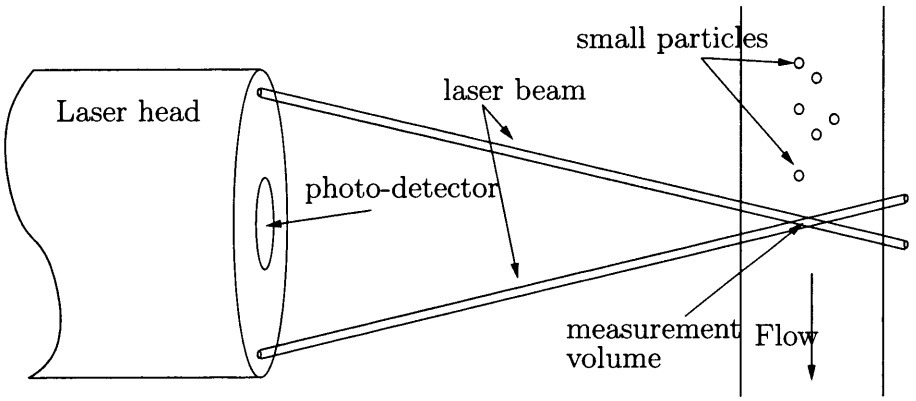

Figure 3.9: *Illustration of a the principle components of a LDV system*

cables provide an easier and safer method, as the plastic around the fibre optic cables removes the danger of laser beams being reflected by intruding obstacles.

LDV offers many advantages over other flow measuring techniques such as propeller meters, acoustic probes, pressure probes or hot-wire anometry. For the purpose of these experiments, the main advantages were the non-intrusive nature of the method (no physical probes are introduced in the water to disrupt the flow) and the accuracy of the measurements.

3.3.3 Particle Imagery Velocimetry

Particle Image Velocimetry (PIV) is one of a number of particle-marker methods that allows for the non-intrusive measurement of a flow field. A more complete review can be read in Adrian (1991). In essence, PIV correlates the displacement of particles between pairs of images to determine the flow velocity vector field. The particle concentration, per image, defines the method of analysis. A low density is called Particle-Tracking Velocimetry (PTV) and a high density is called Laser-Speckler Velocimetry (LSV). PIV correlates patterns within small regions instead of individual particles. The best results are obtained when the particle concentration lies in between PTV and LSV. The particle sizes, usually between 0.1μm and 200μm, and medium (typical artificial particles are: silicon carbide,

glass and nylon) are dependent on the fluid and flow conditions. A laser is the preferred light source as it provides high energy to illuminate the flow particles compared to alternative light sources such as white light.

Illustrations of particle tracking images can be found in Van Dyke (1982). More recent developments in PIV have been made possible by advances in computer technology. With appropriate software, it is now possible to produce quantitative velocity vectors, vorticity fields and shear stresses.

In this investigation, the particles were first submerged in a small amount of wetting agent to avoid any particles coagulating and rising to the surface or creating clumps. There exists some literature by Adrian (1991) and Fincham & Spedding (1997) describing the optimum particle concentration but it has been found that a visual approach provides a good indication of the correct seeding concentration. The calculations to determine the optimum particle concentration are complicated due to the small particle size relative to the test area. It was shown by Adrian (1991) that the actual particle size is not necessarily the size that is displayed by the camera. The particles used in this investigation were 4 microns Nylon particles across an approximate test area of 40cm $\times$ 40cm. The camera, a Powerview 4M Plus, has pixel dimensions 2000 $\times$ 2000. A metric calibration of the field of view reveals that 4-micron particle converts to less than 1 pixel in dimension ($\approx$ 0.02 pixel). However, in the captured images a particle is displayed over a number of pixels. Therefore, a visual approximation is more appropriate in the present experimental set-up.

A number of preliminary tests were carried out to determine the optimum particle medium and concentration in the dense fluid. It was found that Nylon particles (size = 4μm and density = 1.14 grams/cm^3) at a concentration of 0.2 $\times$ 10^{-3} grams/cm, provided a good scatter to produce velocity vectors. The laser was positioned at X = 145cm upstream and at X = $-$145cm downstream from the release point.

The current system uses a Dual YAG pulse laser, with pulse rate set at $7.5Hz$ and camera exposure time of $255\mu s$, to provide flow field illumination. The Pulse PIV system generates the flashing laser light sheet and activates the Powerview 4M Plus camera simultaneously with the aid of a laser pulse synchroniser connected to all the components in the PIV system. The dual laser pulses slightly out of phase and at each laser pulse an image is captured. The time between the laser pulses was set at 0.01s. This value can be set from 1×10^{-6}s to 0.2s. Sufficient time, however, must be allowed for the camera to function and the image to be transferred from the camera to the computer. It is common practice to allow the particles to be displaced between 4 to 8 pixels between two images. The flow velocities in this investigation meant that the experiments were done well within these delta time restrictions.

The post-processing was done with Insight 3G software using a two-pass correlator to compute the flow field parameters. The algorithms and spot size used are given in table 3.3. The pixel vectors were calibrated to give metric velocities with the aid of a 10cm rule placed in the laser sheet plane. A validation stage in processing removed any false vectors. In this investigation, for the gravity current tests, the validation stage removed any vectors outside a velocity range: horizontal -10cm/s to 10cm/s and vertical -5cm/s to 5cm/s.

Variable	Setting
Spot size 1	64 × 64 (pixels)
Spot size 2	32 × 32 (pixels)
Grid engine	Recursive Nyquist grid
Spot mask engine	Gaussian Mask
Correlation engine	Hart Correlator
Peak engine	Gaussian peak

Table 3.3: *Summary of the setting for the PIV software Insight 3G.*

The flow vectors were visualised with the aid of Spatialbox, a specifically de-

signed Matlab 7 Toolbox by TSI. Modifications to the Spatialbox application were made to measure local mean velocities; subtract mean values from the velocity vectors; improve the visualisation of the velocity vectors by skipping velocity vectors in the horizontal and vertical axis; correlating the position of the measurements to the release point; and producing short movies of the PIV measurements.

3.3.4 Laser-Induced Fluorescence

The LIF tests involved a reconfiguration of the PIV system and the Pulnix camera. The laser was set to pulse at 15Hz giving the maximum amount of continuous light and the video capture was set at 30Hz. In this set up, the digital camera and laser pulses were not connected via an electronic synchroniser. This method had the disadvantage that in some cases, the captured images were not in phase with the laser pulse. However, sufficient data was gathered using this method so that this problem was not an important issue. The advantage of the Pulnix camera over the dedicated PIV camera was the ability to generate time-correlated sequences of images. In addition, from the previous work, there already existed a number of developed tools to manipulate and modify the images captured from the Pulnix camera.

Additional analysis tools were developed for the LIF tests to correlate the oscillation of the gravity current with the phase of the wave. This was done by looking at the oscillatory movement of the front of the gravity current. It was assumed that at the instant when the gravity current front started receding, or in some cases not moving forward, this corresponded to the start of the trough of the wave. This gave a time reference from which a correlation between the wave motion and the captured images of the gravity current could be established. The captured images were then compiled to a new sequence of images where only the synchronised frames with the laser pulses were kept.

3.3.5 Acquisition of digital images

A Pulnix TM-9701 high-resolution monochrome 680 × 480 pixel camera was used to measure the evolution with time of the gravity current rate of propagation, the shape of the current head and to determine the density-concentration profiles. The camera was connected via a BNC cable to a Matrox Meteor-II/Standard acquisition card. A traverse of carefully levelled parallel rails, 760cm long, 60cm wide and 120cm high, was designed and built to go along the length of the flume. A trolley with a vertically adjustable mount designed to carry the digital camera was placed on the traverse. A schematic of the equipment is shown in figure 3.10. This allowed the gravity current head to be monitored along the length of the flume.

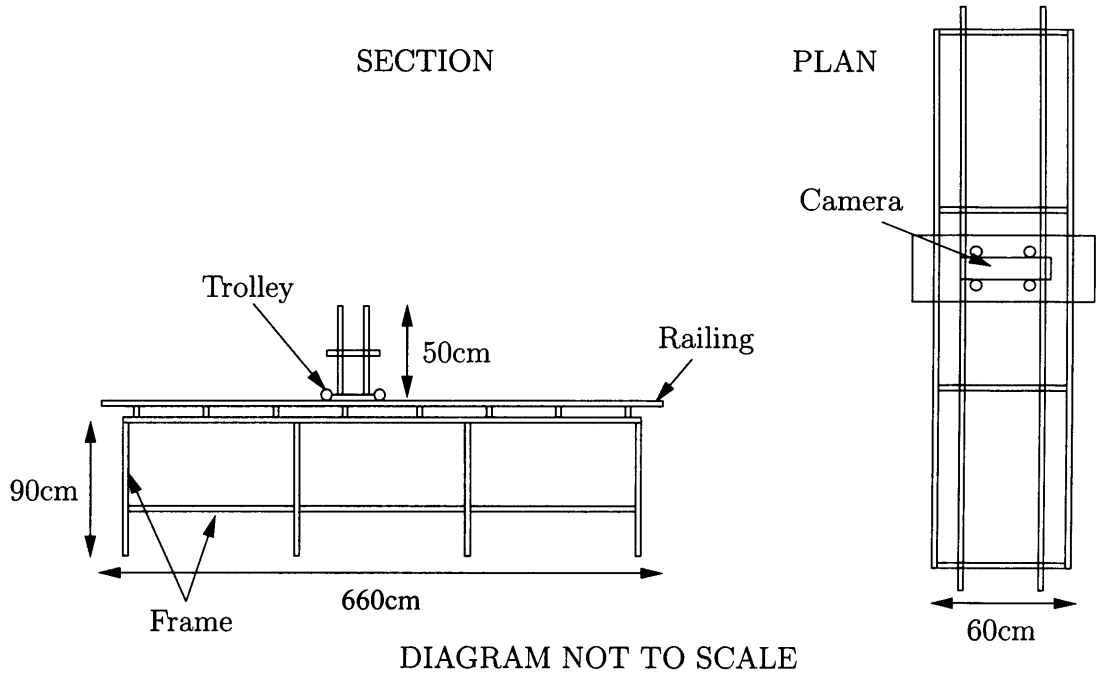

Figure 3.10: *Diagram of the traverse unit.*

A series of light boxes were placed against the opposite glass panels of the flume to provide a uniform background lighting to the gravity current. The light boxes consisted of two 30Watt strip lights inside a reflective coated wooden box (74cm high, 82cm wide and 18cm deep). The front of each box had a 0.2cm thick

white opaque plastic sheet to diffuse the light. This provided a uniform backdrop to the gravity current to analyse the density contours and interface profile with the ambient water.

3.4 Data Analysis

The laboratory tests provided a number of different methods of obtaining information on the wave motion and gravity current dynamics. The gathered measurements from the laboratory tests required new software to be created and adapting existing packages to process the results. Some experimental results are shown in this section. These are for illustrative purposes only and no discussion is given.

The data from the wave probes was acquired with the Foundry Software. The voltage measurements from the wave probes were translated to a water elevation using an in-built Matlab 7 programme. The velocity vectors from the LDV measurement were captured with the use of FIND, software developed by TSI for LDV measurements. The post-processing, to determine the orbital and mean velocities, was done using Matlab 7 programmes.

Image analysis provided quantitative measurements of the propagation, shape and density profile of the gravity current was done through a combination of Matlab 6.5 Image Toolbox and Matrox Inspector programmes. Matrox Inspector software was used to store images from the frame grabber card and offered a number of functions for post processing. The density contours were also analysed with a combination of Matrox Inspector and Matlab 6.5 Image Toolbox programmes.

3.4.1 Wave profile

The free surface wave profiles were obtained from analysis of wave probe measurements, as described in section 3.3.1. The data acquisition sampling rate varied between 200Hz and 500Hz depending on the wave period. In practice, a minimum

of 20 wave cycles was measured and there was a minimum of 100 measurements for each wave cycle. The basic raw data from the four wave probes for one wave cycle are shown in figure 3.11.

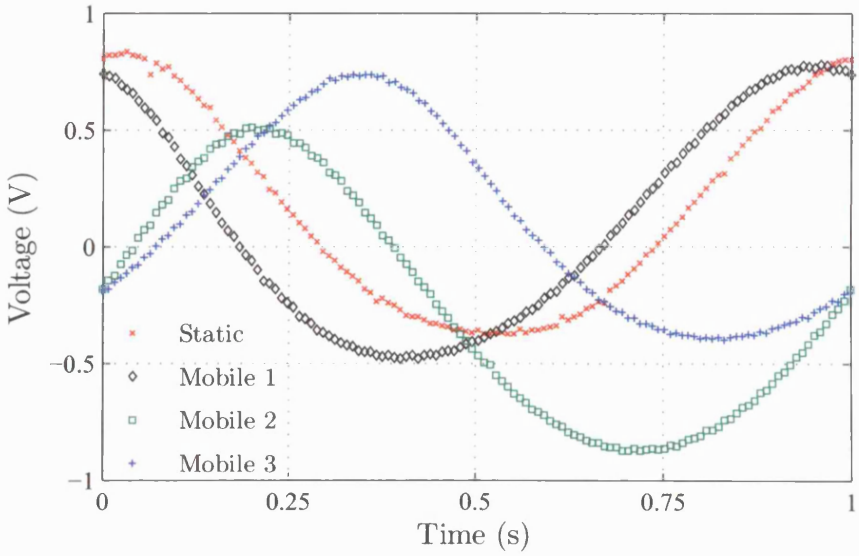

Figure 3.11: *Wave probe measurements over one wave cycle for a 1s wave with an approximate wave height of 6cm.*

The voltage measurements in figure 3.11 can be directly related to water elevation through a simple calibration, where high voltage corresponds to the wave peak and low voltage to the wave trough. A calibration graph was produced by plotting the measured voltages at different water elevations, as illustrated in figure 3.12. The calibration was carried out in a static tank prior to generating the wave profile.

Calculating the correlation coefficient, sometimes also called the cross-correlation coefficient, can test the quality of the data. The method gives a value that corresponds to the quality of a least square fitting to the original data. The value ranges from 1 to 0, where 1 is a perfect match and 0 shows no correlation between data and fitting. For the data in figure 3.12, the correlation coefficients produces values 1 to 0.998. This indicates that the linear approximation is very close to the data values. In this case the wave probes will give an accurate representation of

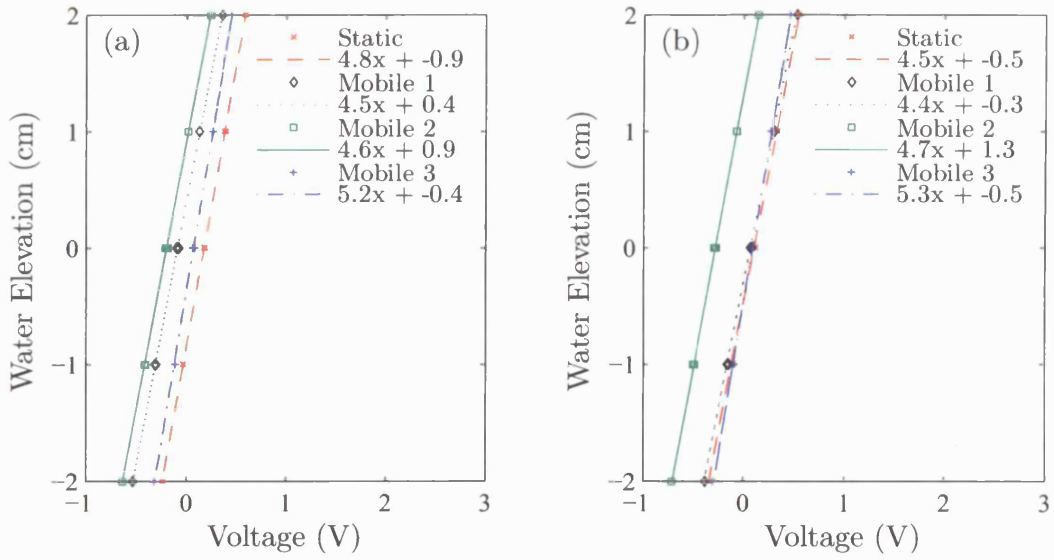

Figure 3.12: *Wave probe calibration graph. Water depth, $d = 40cm$, and water temperature, $T = 17°$ C (a) 01/Dec/04 (b) 02/Dec/04.*

the vertical wave profile over the range of surface elevation used in the calibration. A daily calibration was required as the conductivity of the water may change due to temperature difference and water contamination. This is shown in figure 3.12 where the measurements were taken on two consecutive days.

3.4.2 Ensemble average wave profile

The raw data for one wave cycle show some electric and experimental scatter (figure 3.11). In addition, each wave probe produced different voltage measurements for the same water elevation. Assuming constant wave form along the flume, the true incident wave profile was obtained by taking calibrated ensemble average of the raw data, see figure 3.13.

The first step consists of calibrating the raw data to represent actual water elevations. Following standard procedure, the measurements from the static probe was taken as the phase reference for the measurements from the other four wave probes. An initial scan of the calibrated static measurements locates the positions

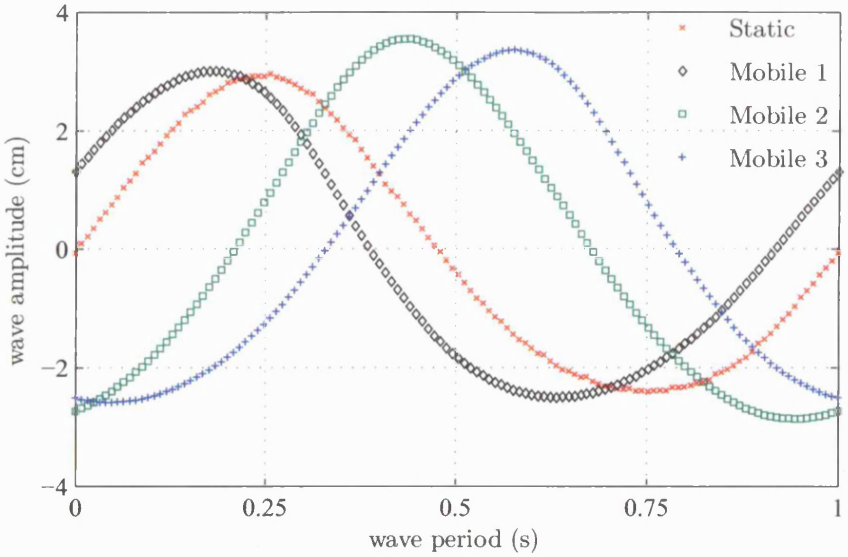

Figure 3.13: *Ensemble average for one wave cycle, 1s wave period and approximate 6cm wave height.*

and times of the sign reversal in the water elevation, from negative to positive, for each wave cycle in the measured data. The number of positions located corresponds to the number of complete wave cycles in the stored data. The data outside this range is truncated.

A second scan of the calibrated data determines average water elevation, corresponding to the position of the sign reversal point in the static probe measurements for each wave probe. The measured ensemble height is dependent on the phase of the wave relative to the static probe measurements. This procedure is repeated for the number of data points in a complete wave cycle (determined by the initial scan). The ensemble average method can be written mathematically for measurements from one probe as:

$$\eta(i) = \frac{1}{n}\sum_{j=1}^{n} \mathcal{D}\left(p(j)+i\right), \tag{3.4.1}$$

where $i = 0, 1, 2, 3 \ldots \text{ndata} - 1$, where ndata is the number of measurements in a complete wave cycle, p is the position of the sign reversal in the data, n is the number of measured wave cycles and $\mathcal{D}$ is the data from a wave probe.

The ensemble average method is used to produce accurate wave profiles of the free surface over one complete wave cycle, as shown in figure 3.13. The wave amplitude from the static probe measurements starts at zero and the phase of the other profiles are relative to the static probe. The relative phase between the wave probes are consistent with the raw data measurements in figure 3.11.

3.4.3 Eulerian measurements of the wave velocity

The wave-induced Eulerian velocities were measured with the use of the LDV system, described in section 3.3.2. The LDV measurements were taken at different positions along a vertical axis at the centre line of the flume and collected data for one hundred thousand data points or a minimum time of 100s at each vertical position. To ensure sufficient scattering particles in the flow for the LDV to operate reliably, small amounts of Titanium (IV) dioxide dust were added to the water. The LDV measurements were used to measure the orbital wave velocities and the mean drift. A typical data sample of the horizontal velocities from one wave cycle is shown in figure 3.14(a) and the ensemble average, from 100 wave cycles, is shown in figure 3.14(b).

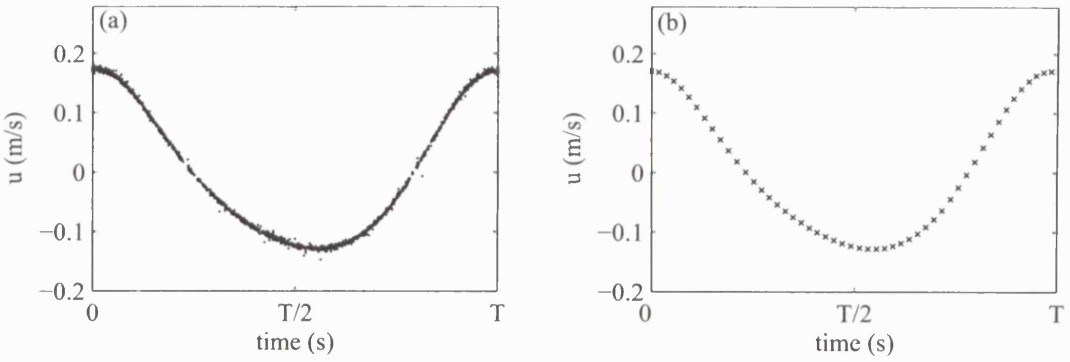

Figure 3.14: *Typical LDV measurements of the horizontal component of the orbital wave velocity below the wave trough. (a) raw data, (b) ensemble average.*

In figure 3.14 the maximum horizontal velocity occurs at the start of the wave period, $t = 0$, and a second maximum at $t = T$. A similar process can be un-

dertaken for the vertical velocity measurements. The measurements of the orbital horizontal velocities, figure 3.14, show an asymmetry in the horizontal velocities. This is conflict with Stokes' higher order wave theory, (2.3.12) and (2.3.19), which are given as a series of even functions in time. The possible reasons for this measured asymmetry is discussed in sections 4.2.2 and 4.3.1.

The LDV measurements above the wave trough did not produce complete orbital velocities (see figure 3.15) due to the intermittent presence of the water, and hence particles, in the wave trough. This induced difficulties in determining the mean velocity in this region. Typical measurements made above the wave trough are shown in figure 3.15(a) and the ensemble average in figure 3.15(b). The velocities above the wave trough have only positive values, this is observed as the net propagation of the wave crests. As this investigation is primarily interested in the propagation of gravity currents at the bed all truncated data measurements are omitted from the wave analysis.

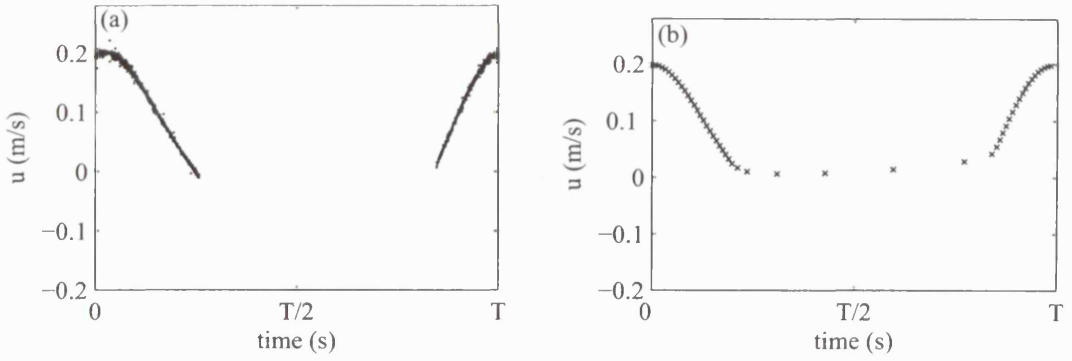

Figure 3.15: *Measured horizontal velocity above the wave trough, over a wave cycle: (a) raw data, (b) ensemble average.*

3.4.4 Location of the gravity current front

The propagation of the gravity current fronts was measured either by simple direct observation or with the use of a video camera. The direct method was the simplest and most convenient technique of recording the displacement of the grav-

ity currents. Two people marked the position of the gravity current fronts at 10s intervals. A metric tape placed on the outside of the glass running the length of the flume gave the position of the markers relative to the point of release. This provided a good approximation of the positions of the current fronts and a simple addition of the downstream and upstream positions determined the overall length of the gravity current. However, in the presence of waves, this method was deemed impractical to study the oscillation of the gravity current front.

A more accurate method of measuring the propagation of the gravity current was by video image analysis. The specifications of the camera and traverse were given in section 3.3.5. The camera was positioned to be level with the bed of the flume and was moved by hand to follow the progression of the gravity current. A typical image of a gravity current front is shown in figure 3.16.

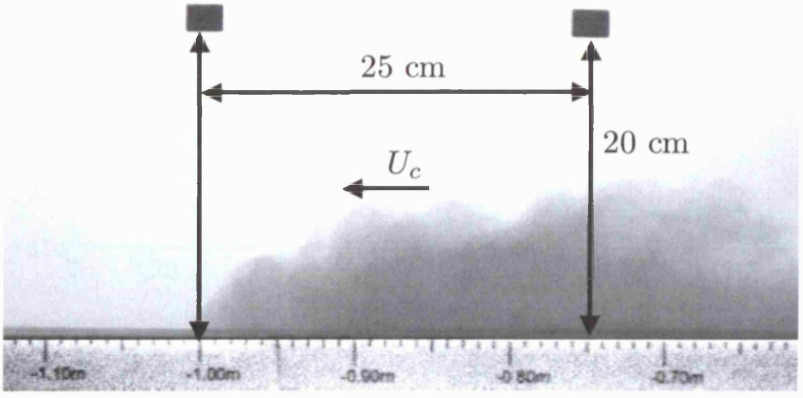

Figure 3.16: *Typical image of a gravity current*

The position of the gravity current front relative to the point of release was determined from black markers placed on the outside of the glass panels. The black markers were placed in such a manner, as they would not obstruct the view of the gravity current. At each measuring window (see section 3.2.3) markers were positioned 25cm horizontally apart and 20cm vertically from the bed of the flume. These dimensions were used to correlate the position and dimensions of the gravity

current. The maximum optical error over the thickness of the glass is negligible (0.17cm). The video and hand measurements were found to differ by a maximum of ±2cm, over the length of a gravity current. This corresponds to an initial maximum error of 8% decreasing to 0.5% at the limits of the measuring section.

The video camera was set to capture 3 frames per second, allowing continuous measurement of the gravity current front position. However, only the images with the black markers in the field of view (see figure 3.16) could be used in the post-processing to determine the location. The measurements plotted in figure 3.17 show the results divided into four test sections by the support frame of the flume (see section 3.2.3).

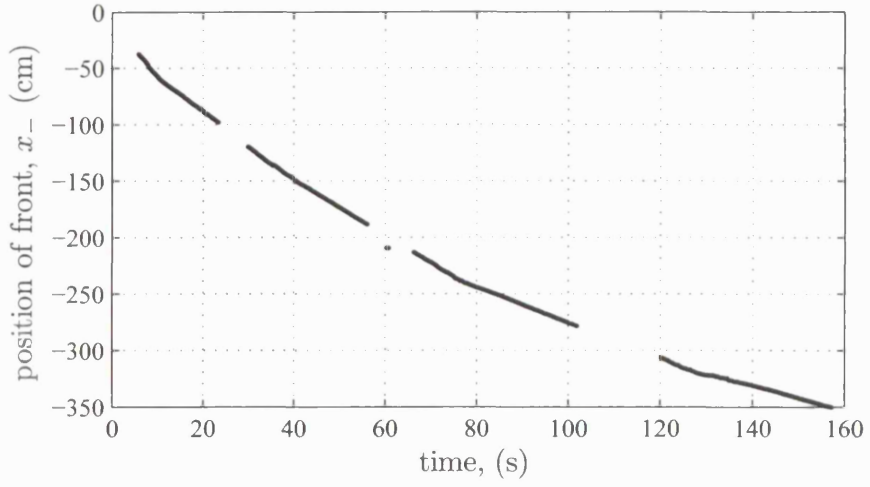

Figure 3.17: *Video measurements of the downstream, x_-, propagation of a gravity current in static ambient water, where $V_0 = 1000cm^3$ and $g_0' = 45cm^2/s$.*

As only one video camera was available, this restricted the image capture to one gravity current front at a time. The video images were used to confirm the direct observations and give detailed analysis of the dynamics at a single gravity current front. However, the overall length of the current was established by combining the video captured measurements in one direction with direct observations in the other.

3.4.5 Gravity current interface with the ambient water

The profile of the gravity current interface was measured by processing the captured images, such as that illustrated in figure 3.16. The size and shape of the gravity current was calibrated with the aid of the two black marks, positioned 25cm apart and 20cm from the bed of the flume.

A routine was written in Matrox Inspector to subtract the background image density and enhance the image contrast. Then a "blob search" was carried out to measure extent of shaded area and hence the height of the gravity current. The "blob search" is an inbuilt Matrox Inspector function able to search for objects of specific light intensity and extract information on the location and size of the object. This procedure can be validated by plotting the calculated interface points with the original images, see figure 3.18. The results show that the method does give an accurate representation of density interface profile between the gravity current and the ambient water at $X = -55$cm ($t = 18$s) and further down the flume at $X = -145$cm ($t = 48$s).

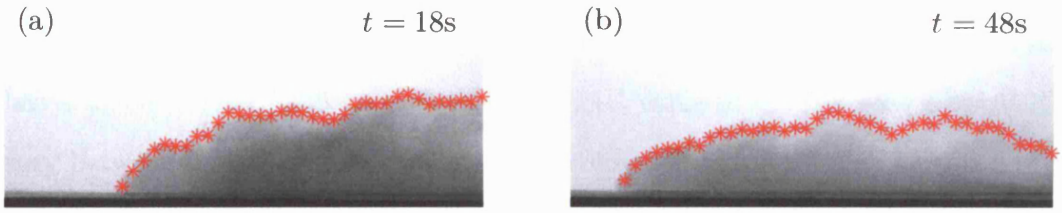

Figure 3.18: *Validation of the calculation of the density interface profile. The measured interface position (∗) overlaid on the video images at t = a) 18s and b) 48s.*

3.4.6 Depth average density profile

Measurement of the density profile within the gravity current head was done by analysis of the attenuation of the background light intensity. Hacker *et al.* (1996) used a similar method to study gravity currents in static ambient water. The

gravity current was distinguished from the ambient water by the use of Potassium Permanganate. On a monochrome camera this appears as black compared to the white/grey background. The concentration of Potassium Permanganate in the saline water controls the background light attenuation. Any mixing with the ambient water decreases the dye concentration and allows more light to pass through the gravity current. In addition, the mixing with the ambient water reduces the density concentration of the gravity current. This correlation between the light attenuation and the density of the gravity current was used to obtain quantitative measurements of the density concentrations averaged over the width of the flume.

The ratio of the negative log of the intensity of the transmitted light, I, to the intensity of the background light, I_0, is called the absorbance. As light passes through a substance the amount of light absorbed depends on the light path length and the concentration of the substance. The classic Lambert-Beer Law describes this mathematically as:

$$-\log\left(\frac{I}{I_0}\right) = \varepsilon bc, \tag{3.4.2}$$

where ε is the extinction coefficient, b path length and c the substance concentration. The light intensities, I and I_0, are measured from the pixel values; black has a pixels value of 255 and white has a pixel value of 0. The grey pixel values vary between 0 and 255, depending on the colour contrast. This resolution can be improved further by adopting double precision processing, converting the integer pixel values to a four decimal places value.

The extinction coefficient, ε, was established by Monk (1963) to vary with the substance concentration, c. An empirical expression of extinction coefficient for Potassium Permanganate was determined by measuring values of $-\log(I/I_0)$ for known path length, b, and dye concentrations, c. An image, with no dye in the water, provides the initial intensity, I_0, and for each dye concentration a new image intensity, I, was taken. The solution concentration was gradually increased by progressively adding small quantities of Potassium Permanganate to the constrained

volume of water. An illustration of the procedure is shown in figure 3.19.

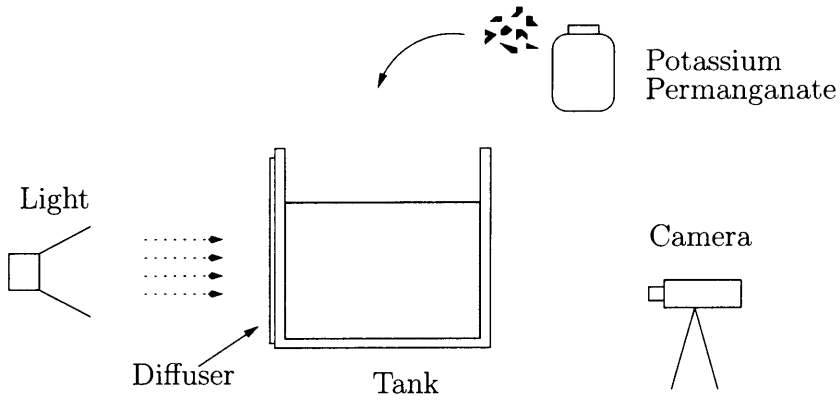

Figure 3.19: *Illustration of the experimental set up for dye calibration.*

It is assumed that the light rays are perpendicular to the sidewalls, so the amount of dye a light ray has passed through is equal to the integral of dye concentration across the width of the channel at the location. A number of calibration tests were carried out in order to determine a mean equation for the extinction coefficient, ε. The sum of the least square method was used (see table 3.4) to determine the appropriate order of the polynomial expression to match the dye calibration measurements.

Order of polynomial :	1	2	3	4	5
Sum of square error :	1.737	0.136	0.046	0.025	0.021

Table 3.4: *Sum of least square method to determine the best approximation to the dye calibration measurements.*

It was found that the third-order polynomial approximation gave a satisfactory best line fit to the data. Higher order expressions produced smaller errors compared to the measurements, however the relatively small improvements did not justify the extra calculations. The measurements of $-\log(I/I_0)$ against the dye concentration per unit width, cb, are shown in figure 3.20 and the third order

approximation is given as:

$$cb = 0.77\mathcal{T}^3 - 0.40\mathcal{T}^2 + 0.36\mathcal{T}, \tag{3.4.3}$$

where $\mathcal{T} = -\log(I/I_0)$ and cb is the concentration per unit width $\times 10^{-3}$.

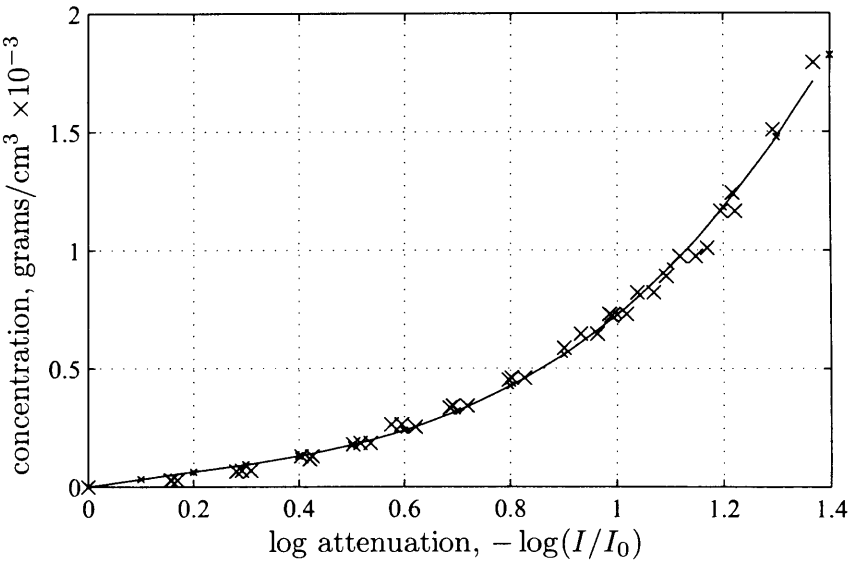

Figure 3.20: *Extinction calibration graph for Potassium Permanganate.*

The correlation, (3.4.3), was then used in the image processing to determine the dye concentration within the gravity current. The video images were used to determine I_0 and I, which were then used with (3.4.3) to determine the dye concentration, an example is shown in figure 3.21.

3.4.7 Mixing Factor

When the dense fluid was released, in this initial stage the dense fluid experiences a high level of mixing with the the ambient water. The mixing factor or dispersion factor is defined as the scaling value from the initial volume to the expanded volume of the released fluid during the initial collapse. In a previous study by Hogg & Huppert (2001), where a similar release method was used, the mixing factor was

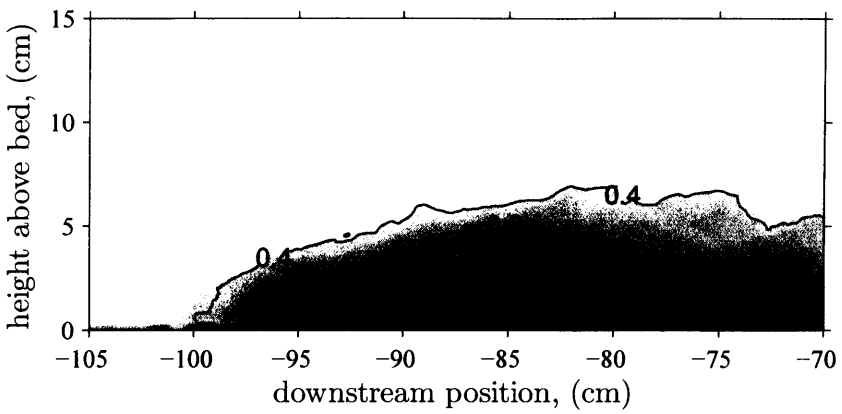

Figure 3.21: *Reduced density contour superimposed on an image of a gravity current, $V_0 = 1000cm^3$ and $g'_0 = 52\ cm/s^2$.*

determined by trapping the released fluid within 30cm and 100cm boundaries of the point of release. Using this method Hogg & Huppert (2001) observed a dispersion factor of 20 during the initial release of the high-density fluid. These experiments were repeated in the current investigation. However, it was found that this method induced excess mixing when the gravity current reached the constraining barriers; and after the dense fluid was allowed to settle, no distinct interface between the dense fluid and ambient water was visible.

In this study the initial entrainment was examined by studying the cross-sectional area during the release. For each image the cross-sectional area was measured using the "blob search" function in Matrox Inspector. An example of the results are summarised in table 3.5.

In this case the dense water, $V_0 = 1800\text{cm}^3$ and $g'_0 = 45\text{cm/s}^2$, was released at the centre of the flume into static water. The mixing factor, $\mathcal{M}$, can be seen in table 3.5 to increase significantly until it reaches a value of 20 ± 2. Hogg & Huppert (2001) measured a similar mixing factor. After that the mixing factor no longer increases significantly, thereafter any further increases in the cross-sectional area were due to the mixing between the gravity current and the ambient water.

Time, (s)	Downstream, x_- (cm)	Upstream, x_+ (cm)	Area, (cm^2)	Volume, (cm^3)	Mixing factor, $\mathcal{M}$
0.00	-4.53	4.77	67	3028	3.0
0.33	-6.80	7.23	194	8845	8.8
0.67	-11.41	12.11	247	11224	11.2
1.01	-15.20	16.23	287	13040	13.0
1.35	-18.44	18.80	307	13958	14.0
1.68	-21.82	21.27	321	14581	14.5
2.01	-23.41	22.91	331	15079	15.1
2.35	-24.41	24.29	382	17403	17.4
2.68	-25.32	25.56	399	18132	18.1
3.01	-26.50	26.77	427	19432	19.4
3.35	-27.32	27.80	457	20778	20.8

Table 3.5: *Mixing factor average over a number of tests:* $V_0 = 1000cm^3$; $g_0' = 52cm/s^2$.

Validation of this process is shown in figure 3.22 at different times during the initial collapse. The top row shows the raw unprocessed images, the middle row the processed images where the cross-section was determined and the bottom row shows the unprocessed images overlaid with the processed images.

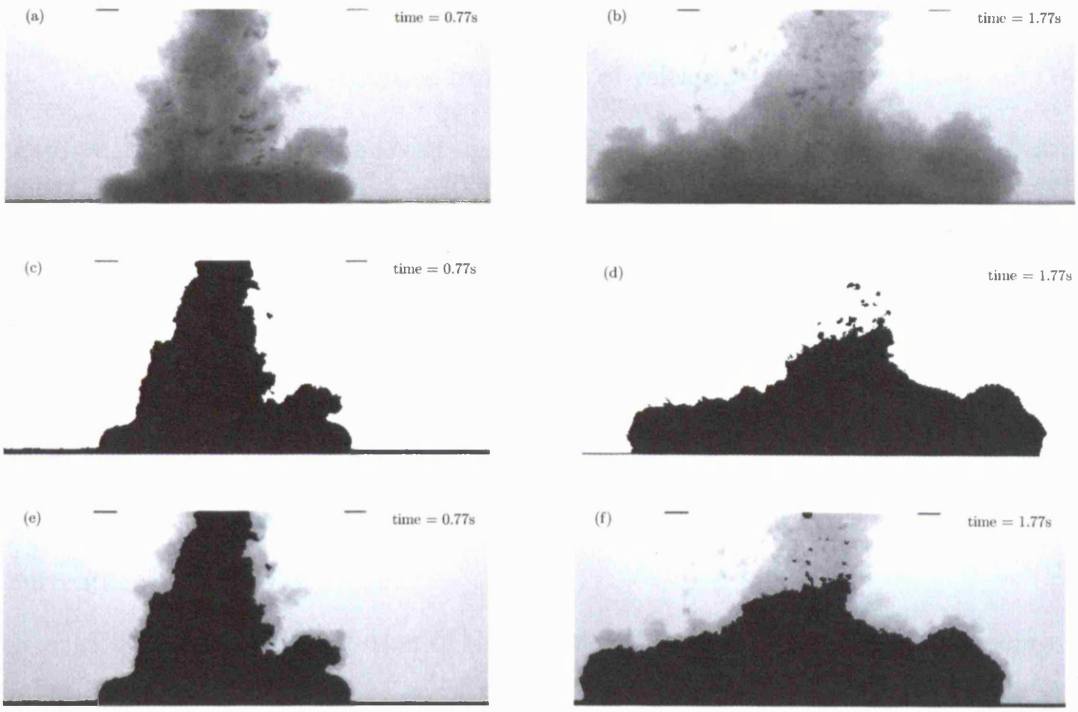

Figure 3.22: *Validation of the mixing factor at a,c,e) $t = 0.77s$ and b,d,f) $t = 1.77s$ during the initial collapse: a,b) raw images, c,d) processed e,f) overlay of raw and processed images.*

There was significant mixing with the ambient water during this initial collapse of the released fluid. This is an important consideration to determine the concentration of the released fluid, and hence the density contrast. The dye concentration is determined by measuring the absorbance, $-\log(I/I_0)$, and calibrating these values with (3.4.3) to give the dye concentration values. The mass of dye, m, is determined by the density concentration, c, where $c = m/V_0$ (see figure 3.23).

The mass measurements in figure 3.23 are much smaller than the initial conditions where the mass, m, was 0.4 grams. This illustrates the entrainment during the initial vertical descent of the gravity current and the significant reduction in the dye concentration. In addition, the mass contours provide further justification

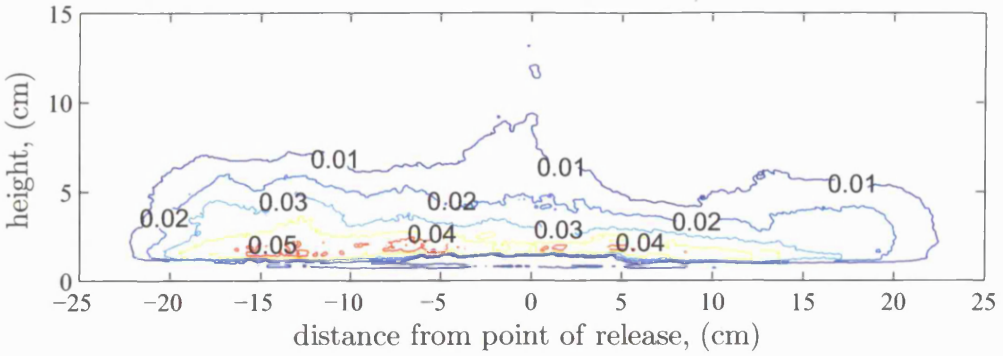

Figure 3.23: *Measured mass of dye during the release of the dense fluid. Initial mass of dye is 0.4 grams.* ($V_0 = 1000cm^3$ *and* $g'_0 = 45cm/s^2$).

for applying a mixing factor, $\mathcal{M}$, of 20, the measured limiting mixing factor in table 3.5. There is a distinct core of the gravity current that shows a mass of 0.02 grams; this corresponds to the initial amount released in the dense fluid taking into account the mixing factor. The vertical descent of the released fluid is an important stage as the initial entrainment controls the horizontal propagation of the gravity current.

A quantitative verification of the calculated entrainment and density contour is shown in figure 3.24, where the density contours have been superimposed on the captured image. The raw image indicates that the released fluid occupies a much larger area than the density contours shows. The mass of dye, m, to the value of 0.02 grams in figure 3.23, is normalised to 1 (yellow density contour) in figure 3.24.

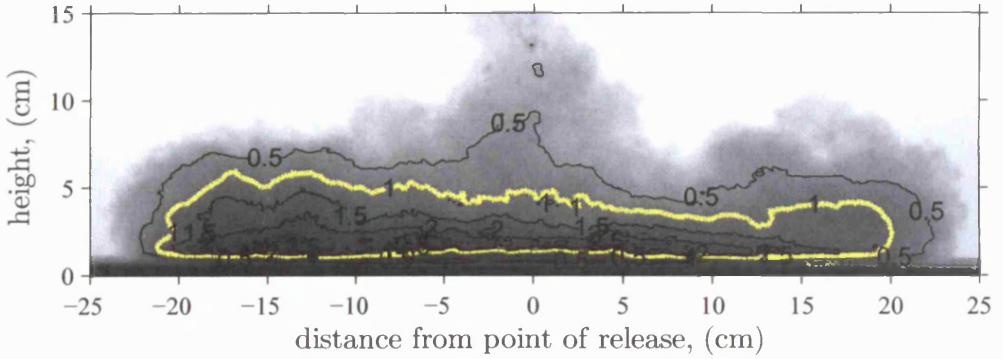

Figure 3.24: *Normalised density contours superimposed on the captured image after the initial vertical entrainment with the ambient water.*

3.4.8 Field of view of the camera

The camera, Pulnix TM 97001, with video tube dimension 0.88cm × 0.66cm ($W_0 \times H_0$) and focal length, l_0, of 1.6cm. The horizontal and vertical angles of divergence, θ_h and θ_v can be determined from the focal length and tube size of the camera. The horizontal and vertical planes of the divergence are of similar geometry. An illustration of the horizontal plane is shown in figure 3.25. A similar diagram could be drawn for the vertical plane.

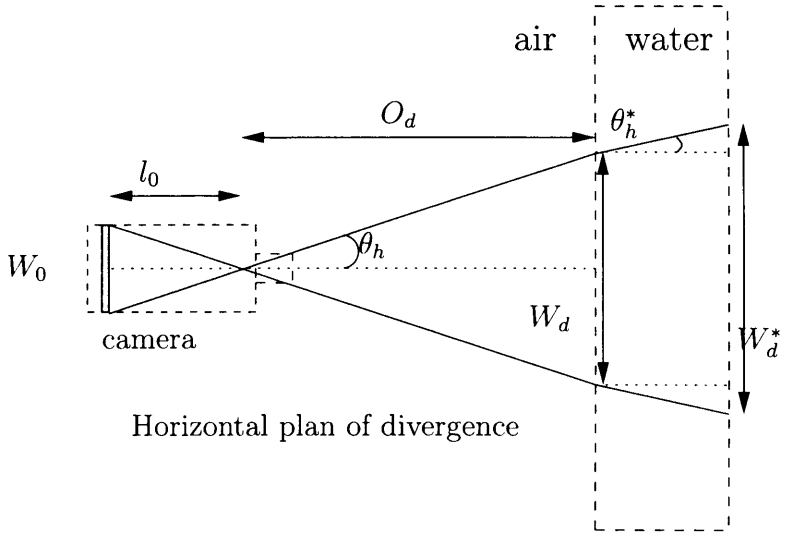

Figure 3.25: *Horizontal field of objective. The divergence angle, θ_h, and the distance, O_d, from the camera to the air/water surface determine the size of the field view at the air/water interface, W_d. This can be used to determine the divergence, θ_h^*, and hence the field of view, W_d^*.*

In air the angle of divergence can be found by simple optical principles. In this case the horizontal, θ_h, and vertical, θ_v, angles are given as:

$$\theta_h = \tan^{-1}\left(\frac{0.5W_0}{l_0}\right) = 15.4^\circ \tag{3.4.4}$$

$$\theta_v = \tan^{-1}\left(\frac{0.5H_0}{l_0}\right) = 11.7^\circ \tag{3.4.5}$$

The size of the field view, $H_d \times W_d$, is dependent on the distance between the camera and objective, defined as O_d in figure 3.25. The reverse is also true and the

distance, O_d, can be given as:

$$O_d = \frac{0.5W_d}{\tan(\theta_h)}, \tag{3.4.6}$$

where the dimensions of the field of view H_d and W_d are determined from the markers placed on the outside of the flume.

In optics, when the light waves travel through different mediums at the boundary the light velocity is altered and changes direction. The effect is dependent on the refractive index of the two materials. The refractive index is well characterised; Tilley (1999) gives the refractive index for air as 1.00, water as 1.33 and crown glass as 1.52. The effect of light waves travelling through water is that the object in the water appears closer than it would if it was in air. Following standard principles, Tilley (1999) expressed the refractive index as:

$$r = \frac{\sin\theta_h}{\sin\theta_h^*} \tag{3.4.7}$$

where θ_h and θ_h^* are the horizontal divergence of two different materials.

Measurement of the field of view dimensions at different positions across the width of the flume is used to determine the horizontal and vertical divergence angles given as θ_h^* and θ_v^* respectively. The result of the increase in the field of view dimension is linearly dependent on the distance from the camera, see figure 3.26. The increase in the horizontal and vertical fields of view dimensions, at different positions across the width of the flume, is shown in figure 3.26.

The linear empirical expressions in figure 3.26 give values of the horizontal refractive angle, θ_h^*, as 10.5° and the vertical angle as θ_v^*, as 7.8°. The expression, (3.4.7), can then be used to give an experimental refractive index value of 1.45 to 1.50 for the combined air/glass/water surfaces. The empirical refractive index is in agreement with the established refractive index for water and glass quoted by Tilley (1999). The experimental measurements confirm the standard values and give a reliable value for the present system.

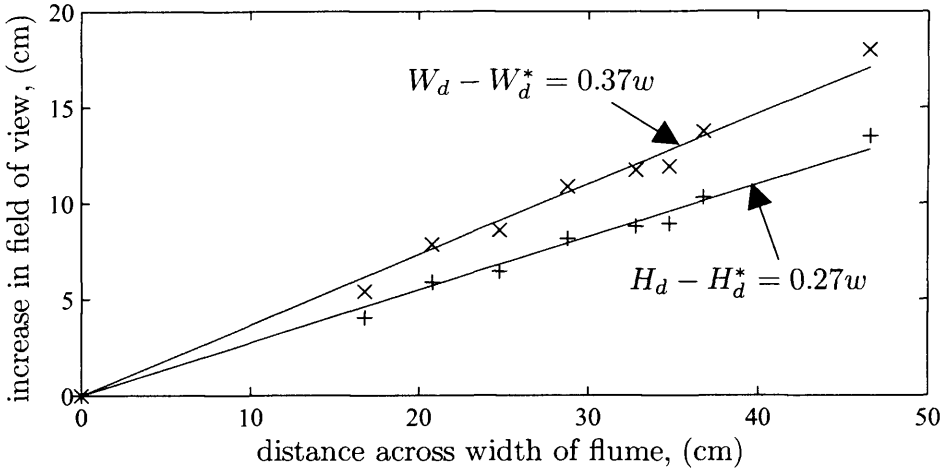

Figure 3.26: *Increase in field view dimensions across the width, w, of the flume.*

3.4.9 Depth of field correction

The width of the flume (the third dimension) can distort the images to give misleading profiles of the gravity current interface with the ambient water. Therefore, care was taken to record the gravity current at bed level; this removed any distortion in the vertical axis. In addition, the distortion in the horizontal axis was removed by ensuring that the centre of the camera never exceeded the front of the gravity current. These two precautions ensured the camera captured true representation of a two-dimensional gravity current front.

However, some consideration needs to be taken of the depth of field effect when measuring the density concentrations of the gravity current head averaged across the width of the flume. The concentration profiles may be significantly altered by the close proximity of the camera to the flume. This can be illustrated by studying the dye calibration images. The Perspex box used for the dye calibration but with no dye is shown in figure 3.27.

The dimensions of the box were 47.5cm long, 27.5cm wide and 45.0cm high. The close proximity of the camera to the objective causes confusion on depth perception. The solid lines show the inside edges of the Perspex box closest to the

Figure 3.27: *Perspex box used for the dye calibration with no dye in the solution: (——) front corners, (- -) back corners.*

camera. The dashed lines are the equivalent edges of the boxes furthest from the camera. The dashed lines are calculated using the divergence theory discussed in section 3.4.8. It can be observed that the calculated corners match up well with the actual back corners in figure 3.27.

With dye solution filling the box, figure 3.28, the visual perception of the depth of field is removed. In this case the Perspex box appears as a flat object. The calculated dashed lines are the only references indicating the back corners of the Perspex box.

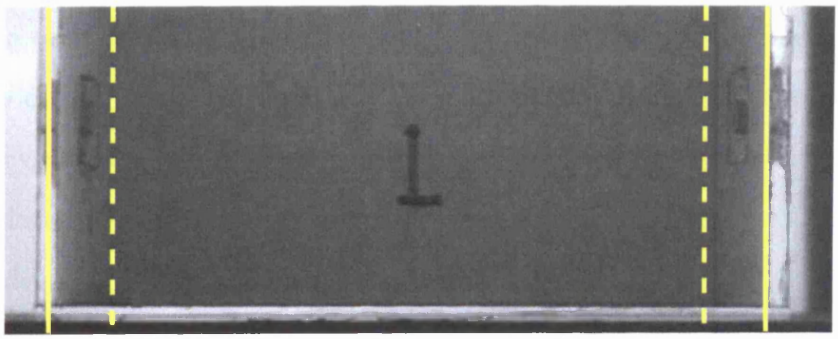

Figure 3.28: *Perspex box used for the dye calibration: with dye.*

The Lambert-Beer, (3.4.2), law predicts that the absorbance is dependent on the light path, b. The theory predicts that between the dashed and solid lines the light attenuation would be smaller than in the central part of the Perspex box. The light paths through the dye solution between back corners marked by

the dashed lines are constant and equal to the width the Perspex. However, at the two extremities, between back and front corners the light paths do not cross the complete width of the box and hence the dye solutions. Analysis of the light attenuation across the length of the Perspex box, figure 3.29, shows that as expected the light attenuation between the solid lines remains constant and at the extremities there is a significant decrease in light attenuation.

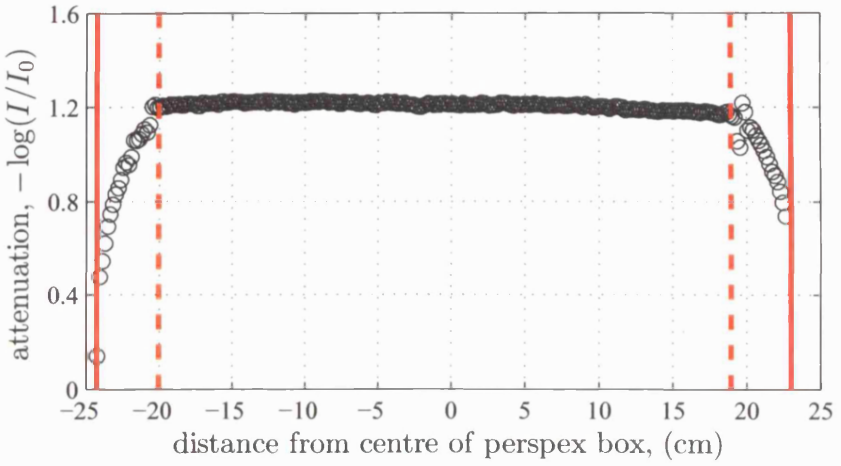

Figure 3.29: *Light attenuation across the Perspex box with uniform dye concentration.*

The decrease in light attenuation, observed at the two extremities in figure 3.29, are due to the shortened path lights through the dye solution. This is in agreement with the theory given in section 3.4.6. The decrease in light attenuation can be plotted against the dye concentration per unit width, figure 3.30, assuming a linear decrease in light paths at the two extremities.

The results in figure 3.30 give a definitive profile and when compared to (3.4.3), the empirical calibration, there is in general good agreement. Therefore it is concluded that the light attenuation relationship (3.4.3) can be used to determine a constant concentration per unit width. However, the results show that for a small light attenuation ($-\log(I/I_0) < 0.4$) the approximation systematically overestimates the concentration. Similar observations were made in section 3.4.6.

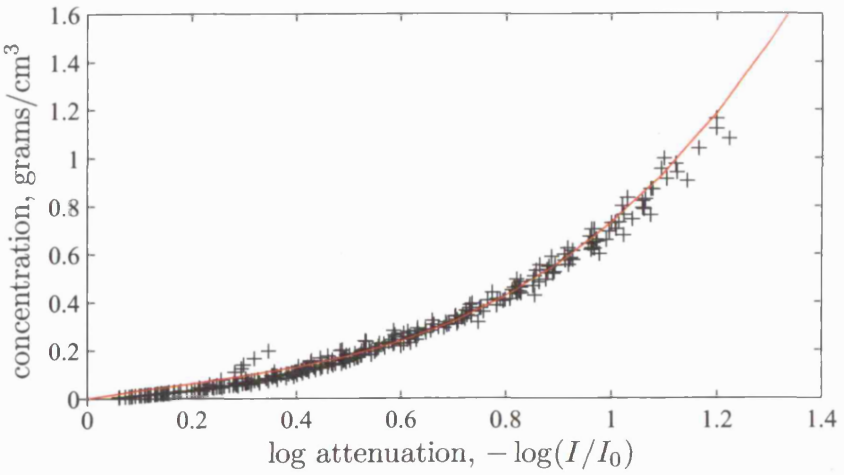

Figure 3.30: *Log attenuation against dye concentration, where the solid line is the theoretical relationship* (3.4.3).

Assuming constant path light, b, between the dashed lines in figure 3.28 and a linear decrease in path length at the two extremities the dye concentration per unit width is shown in figure 3.31. This is shown for a number of different dye concentrations per unit width. In order to compare the concentrations in figure 3.31 with the values in figure 3.30 the concentrations must be multiplied by the depth of the Perspex box.

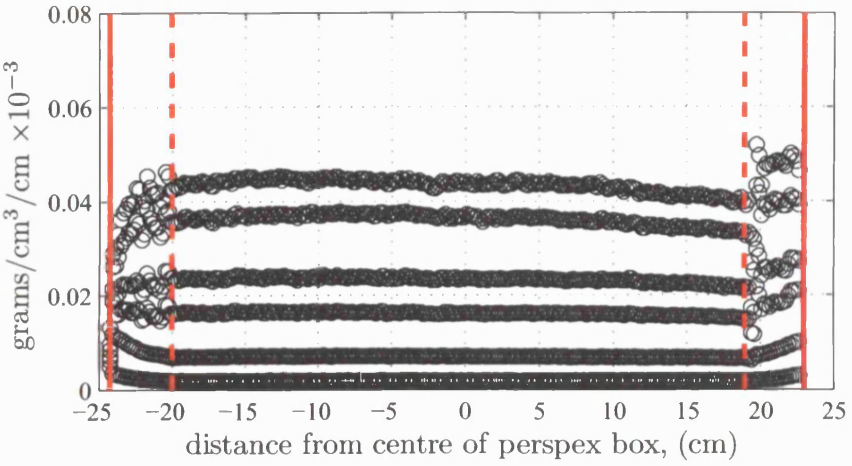

Figure 3.31: *Corrected dye concentration per unit width across a uniform dye concentration solution.*